Water-induced Switching in Selectivity and Steric Control of Activity in Photochemical CO_2 Reduction Catalyzed by RhCp*(bpy) Derivatives

Dongseb Lee, Kosei Yamauchi,* and Ken Sakai*

Department of Chemistry, Faculty of Science, Kyushu University, Motooka 744, Nishi-ku, Fukuoka 819-0395, Japan.

KEYWORDS: *Photocatalytic CO_2 Reduction, Formate Formation, Rhodium Cyclopentadienyl Catalysts, Solar Energy Conversion, Hydrogen Production, DFT Calculations*

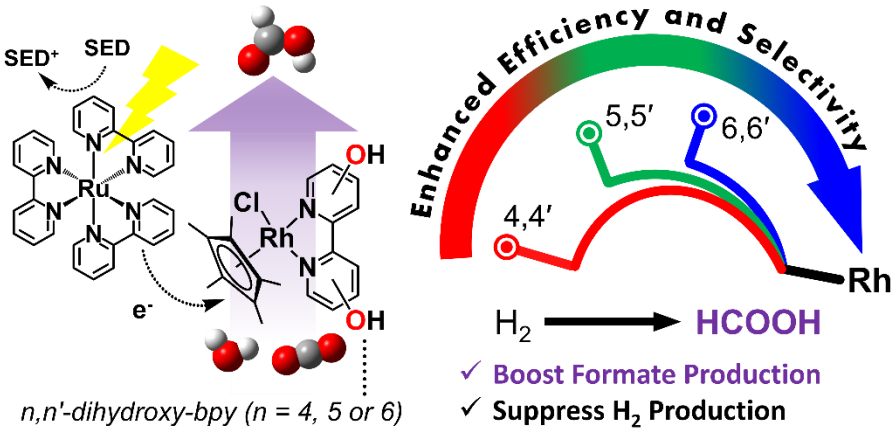

https://doi.org/10.26434/chemrxiv-2024-t3ltd-v3 **ORCID:** https://orcid.org/0000-0003-4976-9796 Content not peer-reviewed by ChemRxiv. **License:** CC BY-NC-ND 4.0

ABSTRACT: Photocatalytic reduction of CO_2 to formic acid (HCOOH) was investigated in either organic or aqueous/organic media by employing three *water-soluble* $[Rh^{III}Cp^*(LH_2)Cl]^+$ (LH_2 = n,n'-dihydroxy-2,2'-bipyridine; n = 4, 5, or 6) in the presence of $[Ru(bpy)_3]^{2+}$, 1,3-dimethyl-2-phenyl-2,3-dihydro-1H-benzo[*d*]imidazole (BIH) and triethanolamine (TEOA). Through studying the electron-donating effects of two hydroxyl groups introduced to the bipyridyl ligand, we found that the substituent positions greatly affect both the catalytic efficiency and selectivity in CO_2 reduction. More importantly, the HCOOH selectivity shows a dramatic increase from 14% to 83% upon switching the solvent media from pure organic to aqueous/organic mixture, where the H_2 selectivity shows a reverse phenomenon. The enhanced HCOOH selectivity and the drastic decrease in the H_2 yield are well rationalized by the fact that the catalytic CO_2 hydrogenation is not only driven photochemically *via* the attack of $Rh^{III}(H)Cp^*(LH_2^{-\bullet})$ on CO_2 but also partly bypassed by a dark H_2 addition reaction yielding $[Rh^{III}(H)Cp^*(L)]^-$ from $[Rh^{III}Cp^*(L)Cl]^+$, which was also separately investigated under the dark conditions. Combination of experimental and theoretical approaches were made to clarify the pK_a values of catalyst intermediates together with the abundant species responsible for the major catalytic processes. Our DFT studies unveil that the exceptionally large structural strain given by the steric contacts between the 6,6'-dihydroxyl groups and the Cp* moiety plays a significant role in bringing about an outstanding catalytic performance of the 6,6'-subsituted derivative. The intrinsic reaction coordinate calculations were carried out to clarify the mechanism of hydride transfer steps leading to generate formate together the heterolytic H_2 cleavage steps leading to afford the key hydridorhodium intermediates. This study represents the first report on the water-induced high selectivity in CO_2-to-HCOOH conversion, shedding a new light on the strategy to control the efficiency and selectivity in the catalysis of CO_2 reduction.

https://doi.org/10.26434/chemrxiv-2024-t3ltd-v3 **ORCID:** https://orcid.org/0000-0003-4976-9796 Content not peer-reviewed by ChemRxiv. **License:** CC BY-NC-ND 4.0

INTRODUCTION

By following the Paris agreement,[1] greenhouse gas emission must be substantially suppressed by replacing fossil fuels with sustainable energy sources. Inspired by the natural photosynthesis of green plants, artificial photosynthesis converting sunlight into carbon neutral fuels has attracted great attention towards the development of clean as well as renewable energy cycles. Up to now, extensive efforts have been made to advance the chemistry of catalytic CO_2 reduction into chemical fuels such as HCOOH, CO, MeOH, and CH_4.[2-4] The studies involve both photocatalysis and electrocatalysis of CO_2 reduction into value-added chemical fuels. Among various approaches, homogenous catalysis using transition metal molecular systems have attracted a great deal of attention due to the well-defined structures enabling researchers to examine and establish the structure-activity relationships. The detailed studies on such issues may lead to realization of the factors that govern the catalytic property of individual molecular systems. Moreover, the extended studies may lead to provide the mechanistic insights correlated with the catalytic efficiency and selectivity.[5-8] In general, we suffer from the concomitant generation of multiple reduction products, such as HCOOH, CO, and H_2. Therefore, it is extremely important to explore rational strategies to control the product selectivity in CO_2 reduction.

In the above context, one of our recent interests has concentrated on the selective formation of HCOOH (or formate) due to its potential application in reversible hydrogen energy storage technology.[9] The selective formate production is particularly important in order to fabricate the high-pressure H_2 gas generation technology required to operate the hydrogen fuel cells in various purposes; HCOOH → H_2 (high pressure) + CO_2 (liquid).[10] As far as our literature search results are concerned, examples of catalysts as well as conditions enabling the selective formation of HCOOH in CO_2 reduction, especially in the presence of a proton source, is quite limited.[11,12] In contrast, the majority of reports demonstrate selective formation of CO rather than HCOOH,[13] which is often due to the predominant formation of metal-carbon-bonded CO_2^{2-}-bound species, as described elsewhere.[8,14-16] Although the formate ($HCOO^-$) formation has been often described to take place *via* the insertion of CO_2 into a metal-hydride bond (Type A in Scheme 1),[17] recent theoretical studies including this work well demonstrate that this

https://doi.org/10.26434/chemrxiv-2024-t3ltd-v3 **ORCID:** https://orcid.org/0000-0003-4976-9796 Content not peer-reviewed by ChemRxiv. **License:** CC BY-NC-ND 4.0

definition is rather misleading since formate generally forms *via* the nucleophilic attack of a metal-hydride (M-H) at the carbon center of CO_2 (Types B-D in Scheme 1),[18-20] with minor exceptions.[21] In other words, the hydride on a metal behaves as a nucleophilic attacker as far as it is hydridic enough to stabilize the transition state of reaction. In the earlier studies while lacking the DFT approach, the O(formate)-coordinated structures solved by X-ray diffraction directed researchers to define the pathway called "CO_2 insertion into a M-H bond".[22] Later, the DFT calculations by Ahlquist[18] and Hazari[19] revealed the two-step pathways triggered by (i) the M-H attack to CO_2 followed by (ii) the transformation into the O(formate)-coordinated catalyst (Type B in Scheme 1). Nevertheless, such two-step pathways are only applicable to the catalysts which can stabilize the M-O(formate) bond after releasing the hydride. Moreover, it still remains ambiguous whether the so-called CO_2-insertion products are actually given *via* the intervention by solvent or other coexisting donors in solution (Type C_1+C_2 in Scheme 1). Considering the hydricity high enough to afford formate, the metal center releasing the hydride may possess a kinetically labile character leading to allow ligand substitution in a high rate. Moreover, an increasing number of reports have recently evidenced direct release of formate *via* the M-H attack with the lack of any O(formate)-coordinated products (Types C_1 or D in Scheme 1).[20,23] The present study further demonstrates that the CO_2 reduction to formate undergoes *via* the nucleophilic attack of a metal hydride and directly ends up with the release of formate (Type D in Scheme 1).

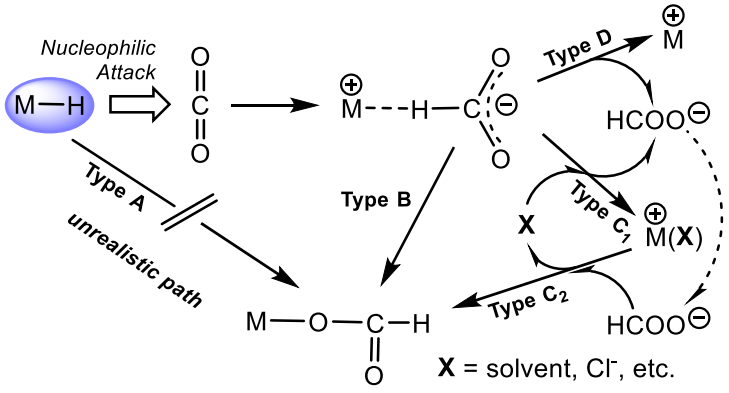

Scheme 1. Possible reaction pathways to form formate *via* the attack of a metal hydride: CO_2 insertion (Type A), M-H attack followed by direct M-O(formate) bond formation (Type B); M-H attack followed by both ejection of formate and donation of X (Type C_1 or C_1+C_2), and M-H attack followed by ejection of formate (Type D), where Type C_1+C_2 denotes the M-H attack followed by indirect M-O bond formation *via* intervention by a coexisting donor X.

https://doi.org/10.26434/chemrxiv-2024-t3ltd-v3 **ORCID:** https://orcid.org/0000-0003-4976-9796 Content not peer-reviewed by ChemRxiv. **License:** CC BY-NC-ND 4.0

The family of **RhCp*(bpy)** derivatives are of particular interest. Marc Fontecave *et al.* previously developed a series of $[Rh^{III}Cp^*(R,R\text{-bpy})Cl]^+$ catalysts with a variety of substituents on the R,R-bpy, demonstrating the tunability in the CO_2 reduction yield together with the selectivity in HCOOH versus H_2 formation.[23d] Using a non-aqueous photocatalytic system driven by the standard $[Ru(bpy)_3]^{2+}$ photosensitizer (5:1 v/v, MeCN/TEOA mixture, where MeCN is acetonitrile), they were able to control the HCOOH/H_2 production ratio in the range of 0.29-1.36. On the other hand, our recent studies have continued to persist in the use of aqueous media with the aim of fabricating truly environmentally friendly photocatalytic systems free of any risks towards the emission of organic pollutants into the atmosphere.[24] However, the suppression of water reduction to H_2 in aqueous media is in principle challenging since the water reduction is thermodynamically more feasible relative to the CO_2 reduction. Nevertheless, we could previously demonstrate how the selectivity in CO_2 reduction versus H_2 evolution can be maximized up to ca. 90% in fully aqueous carbonate buffer at pH 6.7 by employing water-soluble cobalt porphyrins as CO_2 reduction catalysts.[8,15] The successful suppression of water reduction to H_2 was also attributed to the lack of any effective proton relaying species, such as $H_2PO_4^-$ available in a pH 7.0 phosphate buffer.[25] Nevertheless, we were somewhat disappointed with the fact that the cobalt porphyrin catalysts all exhibit 100% selectivity in CO versus HCOOH formation. Thus, the catalysis of selective HCOOH formation in fully aqueous media is still quite limited, except for the

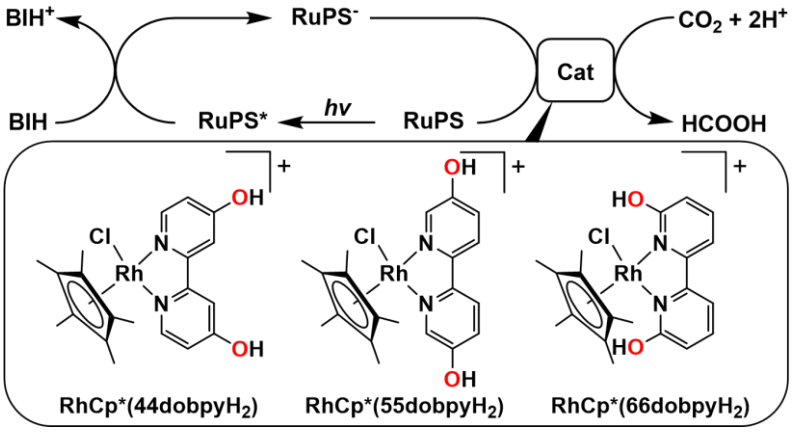

Scheme 2. Photocatalytic CO_2 reduction system made up of a **RhCp*(dobpyH$_2$)** derivative as a catalyst, $[Ru(bpy)_3]^{2+}$ as a photosensitizer (RuPS), and BIH as a sacrificial electron donor (Figure S1).

https://doi.org/10.26434/chemrxiv-2024-t3ltd-v3 **ORCID:** https://orcid.org/0000-0003-4976-9796 Content not peer-reviewed by ChemRxiv. **License:** CC BY-NC-ND 4.0

Ru(II)-Re(I) supramolecular catalyst which was proven to be highly selective towards formate formation in aqueous solution.[12a] In the above context, we have investigated the catalytic CO_2 reduction properties of water-soluble **RhCp*(dobpyH$_2$)** derivatives shown in Scheme 2 in our hope to obtain highly selective formate formation systems operatable under aqueous conditions. Here dobpyH$_2$ denotes the family of 4,4′-, 5,5′-, and 6,6′-dihydroxy-2,2′-bipyridine, which will be abbreviated as 44dobpyH$_2$, 55dobpyH$_2$, and 66dobpyH$_2$, respectively, where dobpy denotes dioxobipyridine. The ligand will also be abbreviated as LH$_2$ where necessary. As depicted in Scheme 2, the catalysts bearing these ligands will be abbreviated as **RhCp*(44dobpyH$_2$)**, **RhCp*(55dobpyH$_2$)**, and **RhCp*(66dobpyH$_2$)**, respectively. Among them, **RhCp*(44dobpyH$_2$)** is a reported compound which was previously investigated for its catalytic activity (not photocatalytic) towards the hydrogenation of CO_2 into HCOOH,[26] while the remainders are new compounds. In this study, the effect of substituent positions as well as the effect of adding water on the photocatalytic efficiency and product selectivity are examined in detail with our special attention paid to the selectivity in HCOOH formation. In addition, possible reaction pathways for all three catalysts are proposed by developing the free energy diagrams computed by the density functional theory (DFT) calculations. Moreover, the structure-activity relationships are established based on our careful examinations into the experimental and theoretical results. The most remarkable finding in this report lies in the drastic change in the product selectivity induced by switching the reaction media from non-aqueous to aqueous/organic phase, leading to demonstrate outstanding efficiencies of these catalysts in the CO_2-to-HCOOH conversion. We also note that our results on the **RhCp*(dobpyH$_2$)** must be viewed as related to the previous report on the IrCp*(bpy) catalysts studied for their activity towards the CO_2 hydrogenation.[27]

https://doi.org/10.26434/chemrxiv-2024-t3ltd-v3 **ORCID:** https://orcid.org/0000-0003-4976-9796 Content not peer-reviewed by ChemRxiv. **License:** CC BY-NC-ND 4.0

RESULTS AND DISCUSSION

Electrochemical Properties

To clarify the fundamental electrochemical and electrocatalytic properties of the **RhCp*(dobpyH$_2$)** family, the cathodic polarizations were initially made for the anhydrous dimethylformamide (DMF) solution of the individual catalyst under either Ar or CO_2 atmosphere (Figure 1), in which both the square wave voltammetric (SWV) and cyclic voltammetric (CV) techniques were adopted to fully understand the relevant properties. Catalyst **RhCp*(44dobpyH$_2$)** displays two distinct reduction peaks at -0.70 V and -0.79 V vs. Fc/Fc$^+$, assignable to the $Rh^{III/II}$ and $Rh^{II/I}$ reduction processes. On the other hand, both **RhCp*(55dobpyH$_2$)** and **RhCp*(66dobpyH$_2$)** exhibit a single 2-electron reduction peak attributable to the $Rh^{III/I}$ couple appearing at -0.89 V and -0.94 V, respectively, as described elsewhere.[23d,28] The observed cathodic shift in the 2-electron reduction potential in the latter is indicative of the increased electron density at the metal center, likely due to the stronger electron-donating property of the 6,6'-dihydroxyl rather than the 5,5'-dihydroxyl groups because of the closer location of the groups with regard to the metal-bonded nitrogen centers. Although exact assignments of multiple reduction waves appearing at the more cathodic domain beyond ca. -1.4 V remain unexplored, these reduction waves are assignable to the bpy-based reduction leading to afford the $[Rh^{I}Cp^*(dobpyH_2^{\bullet-})]^-$ species. It may be due to the presence of unidentified multiple $Rh^{I}Cp^*(dobpyH_2)X$ species, for instance, due to the difference in the X ligand (e.g., X = Cl$^-$, DMF, etc.). It should be noted that our DFT results deny the two-step 1-electron reductions of the dobpyH$_2$ ligand leading to afford the $[Rh^{I}Cp^*(dobpyH_2^{2-})]^{2-}$ species (data not shown).

Upon purging CO_2 into the electrolysis solution, all systems show enhanced current attributable to the electrocatalytic CO_2 reduction at around the dobpyH$_2$-based reduction potentials regardless of the presence of water. For all catalysts, the overpotential for the electrocatalytic CO_2 reduction ($E_{cat/2}$) remains unaffected by the presence of water. However, only catalyst **RhCp*(66dobpyH$_2$)** exhibits a significant enhancement in the catalytic current upon addition of water, which is in line with the enhanced photocatalytic CO_2 reduction rate of this catalyst under the similar experimental conditions

https://doi.org/10.26434/chemrxiv-2024-t3ltd-v3 **ORCID:** https://orcid.org/0000-0003-4976-9796 Content not peer-reviewed by ChemRxiv. **License:** CC BY-NC-ND 4.0

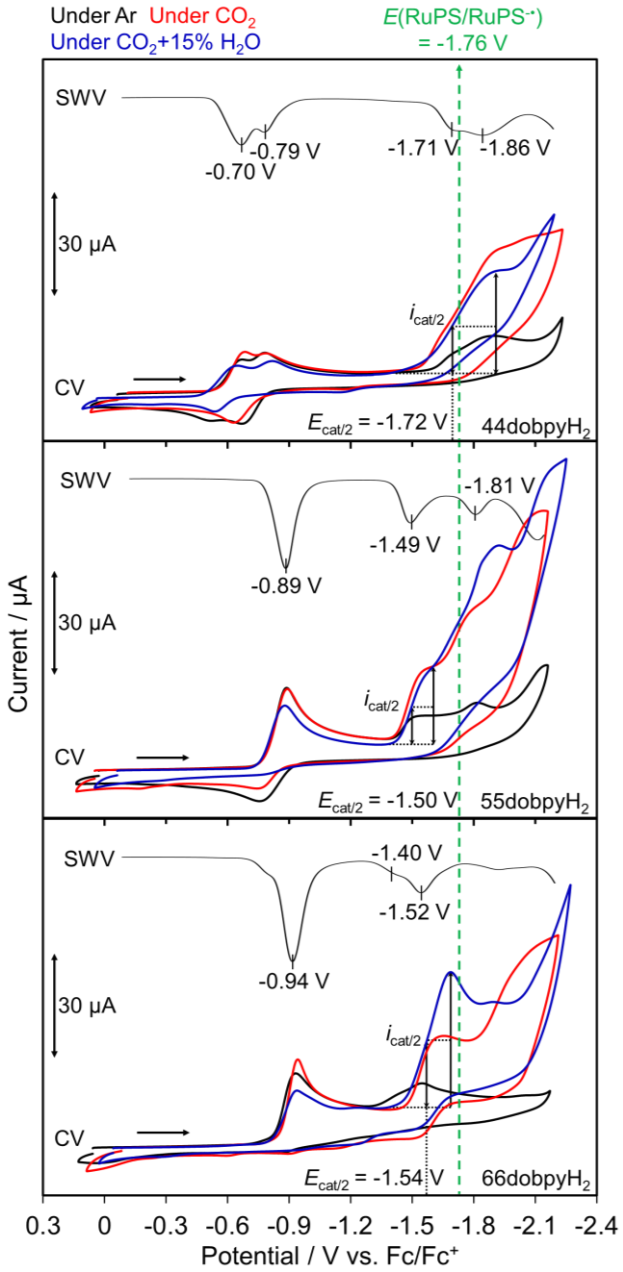

Figure 1. SWV and CV data recorded for the solutions of **RhCp*(dobpyH$_2$)** (1.0 mM) at the scan rate of 100 mV/s. The measurements were conducted for the Ar- or CO_2-saturated DMF solution (black or red) and the CO_2-saturated DMF+H_2O (85:15 v/v) mixture (blue). The both solutions contain TBACl (0.1 M; TBA^+ = tetra(n-butyl)ammonium) as a supporting electrolyte. The working, counter, and reference electrodes are glassy carbon, Ag/Ag^+, and Pt wire electrodes, respectively. The green dashed line represents the reduction potential of $[Ru(bpy)_3]^{2+}$.[29,30] The insets show the magnification around the rise of catalytic current for CO_2 reduction.

(see below). By analogy to the similarity in the Rh-based reduction profiles (see above), the $E_{cat/2}$ values for **RhCp*(55dobpyH$_2$)** and **RhCp*(66dobpyH$_2$)** (ca. -1.50~ -1.54 V) are both positive-shifted relative to that of **RhCp*(44dobpyH$_2$)** (-1.72 V). Using these $E_{cat/2}$ parameters, the *formal* driving force

https://doi.org/10.26434/chemrxiv-2024-t3ltd-v3 **ORCID:** https://orcid.org/0000-0003-4976-9796 Content not peer-reviewed by ChemRxiv. **License:** CC BY-NC-ND 4.0

for the electron transfer (ΔE) when promoting the CO_2 reduction by the photochemically produced reducing equivalents (*i.e.*, $[Ru(bpy)_2(bpy^{-\bullet})]^+$) can be discussed as follows. By employing the reduction potential for the $[Ru(bpy)_3]^{2+}/[Ru(bpy)_2(bpy^{-\bullet})]^+$ couple (E_{red} = -1.76 V vs. Fc/Fc^+), each ΔE can be estimated according to $\Delta E = E_{cat/2} - E_{red}$. As illustrated in Figure 1, **RhCp*(55dobpyH₂)** and **RhCp*(66dobpyH₂)** possess higher values in ΔE (220-260 mV) compared to that of **RhCp*(44dobpyH₂)** (ca. 40 mV). These results can be correlated with the photocatalytic CO_2 reduction rates described below for these catalysts.

On the other hand, one can further recognize that the CV profiles for the catalytic CO_2 reduction are roughly classified into two groups. The electrocatalysis seems triggered after promoting the dobpyH₂-reduction step when catalyzed by **RhCp*(44dobpyH₂)** and **RhCp*(55dobpyH₂)**, while the overpotential for the electrocatalysis by **RhCp*(66dobpyH₂)** is obviously shifted to the potential which is effectively more cathodic to the dobpyH₂-based reduction potential observed in the absence of CO_2 (see Figure 1). In other words, the CV profiles for the electrocatalysis by **RhCp*(66dobpyH₂)** clearly lack the dobpyH₂-based reduction profiles characteristic of the $Rh^{I}Cp^*$(66dobpyH₂) intermediate produced at -0.94 V in the absence of CO_2. These results suggest that the $Rh^{I}Cp^*$(66dobpyH₂)

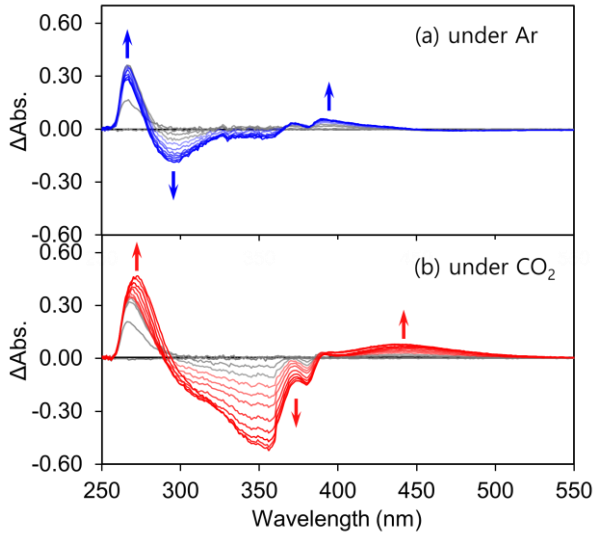

Figure 2. UV-Vis SEC data for the DMF solution of **RhCp*(66dobpyH₂)** (1.0 mM) in the presence of TBACl (0.1 M) applied at -1.0 V vs. Fc/Fc^+ at 20 ºC by employing platinum mesh working electrode under Ar (top) and CO_2 (bottom). The interval between measurements is 200 seconds.

https://doi.org/10.26434/chemrxiv-2024-t3ltd-v3 **ORCID:** https://orcid.org/0000-0003-4976-9796 Content not peer-reviewed by ChemRxiv. **License:** CC BY-NC-ND 4.0

intermediate reacts with CO_2 to give a different chemical species while conducting the cathodic polarization beyond -0.94 V. In order to confirm the validity of this hypothesis, spectroelectrochemical (SEC) studies were carried out for all **RhCp*(dobpyH$_2$)** derivatives using the conditions used to measure the electrochemical data shown in Figure 1. By holding the working electrode potential at -1.0 V, corresponding to the potential completing the Rh^{III}/Rh^{I} reduction for all catalysts, UV-visible spectral changes in either Ar or CO_2 atmosphere were observed every 200 s (Figures 2 and S9). Under Ar atmosphere, all catalysts show spectral changes attributable to the formation of the Rh^{I}Cp*(dobpyH$_2$) intermediate (Figures 2a and S9). An important finding is that the time-course of spectral changes are drastically affected by introducing CO_2 only when the **RhCp*(66dobpyH$_2$)** derivative is adopted (Figure 2b). In contrast, the spectroelectrochemical behaviors of **RhCp*(44dobpyH$_2$)** and **RhCp*(55dobpyH$_2$)** are clearly insensitive to the exposure to CO_2 (Figure S9), implying the lack of their driving force to promote the formal CO_2-to-CO_2^{2-} reduction by the Rh^{I}/Rh^{III} couple, *i.e.*, $Rh^{I} + CO_2 \rightarrow Rh^{III}(CO_2^{2-})$, because of the anodically shifted potentials for their Rh^{III}/Rh^{I} couples (-0.70~ -0.89 V) relative to that of **RhCp*(66dobpyH$_2$)** (-0.94 V). The new species given in the reaction of Rh^{I}Cp*(66dobpyH$_2$) with CO_2 is featured by the bleach and growth of absorption at 350 and 450 nm, respectively, even though the actual species given remains unclarified in this report. Nevertheless, our results clearly reveal the difference in reactivity of these two classes of catalysts. As far as the electrocatalysis is concerned, it is considered that an unidentified species is given *via* the reaction of Rh^{I}Cp*(66dobpyH$_2$) and CO_2 prior to the dobpyH$_2$-based reduction. On the other hand, the $[Rh^{I}Cp^{*}(dobpyH_2^{-\bullet})]^{-}$ species must be generated to trigger the catalysis of either CO_2 or water reduction when **RhCp*(44dobpyH$_2$)** and **RhCp*(55dobpyH$_2$)** are adopted. However, under the photocatalytic conditions in which a substantially different solvent mixture is used, the $Rh^{III}(CO_2^{2-})$ species does not play a significant role in catalysis since the CO expected to be produced from this species is a minor product, less than 1% in selectivity (see below).

https://doi.org/10.26434/chemrxiv-2024-t3ltd-v3 **ORCID:** https://orcid.org/0000-0003-4976-9796 Content not peer-reviewed by ChemRxiv. **License:** CC BY-NC-ND 4.0

Photocatalytic CO_2 reduction

Photocatalytic CO_2 reduction performances were investigated using the CO_2-saturated solutions prepared by using a mixed solvent consisting of either MeCN+TEOA (5:1 v/v) or MeCN+H_2O+TEOA (4:1:1 v/v). The use of the latter solvent mixture allows us to understand the role of water in the product yield and selectivity. The photolysis solutions contained each **RhCp*(dobpyH$_2$)** derivative (0.1 mM) as a catalyst, $[Ru(bpy)_3]^{2+}$ (1.0 mM) as a photosensitizer, and BIH (1,3-dimethyl-2-phenyl-2,3-dihydro-1H-benzo[*d*]imidazole; 0.1 M) as a sacrificial electron donor. Importantly, TEOA in each mixed solvent serves as a proton relay to abstract the proton of BIH^+ to avoid the backward electron transfer from $[Ru(bpy)_2(bpy^{-\bullet})]^+$ (*i.e.*, TEOA + H^+ ⇌ $[TEOA(H)]^+$; pK_a = 15.9 in acetonitrile) rather than a sacrificial

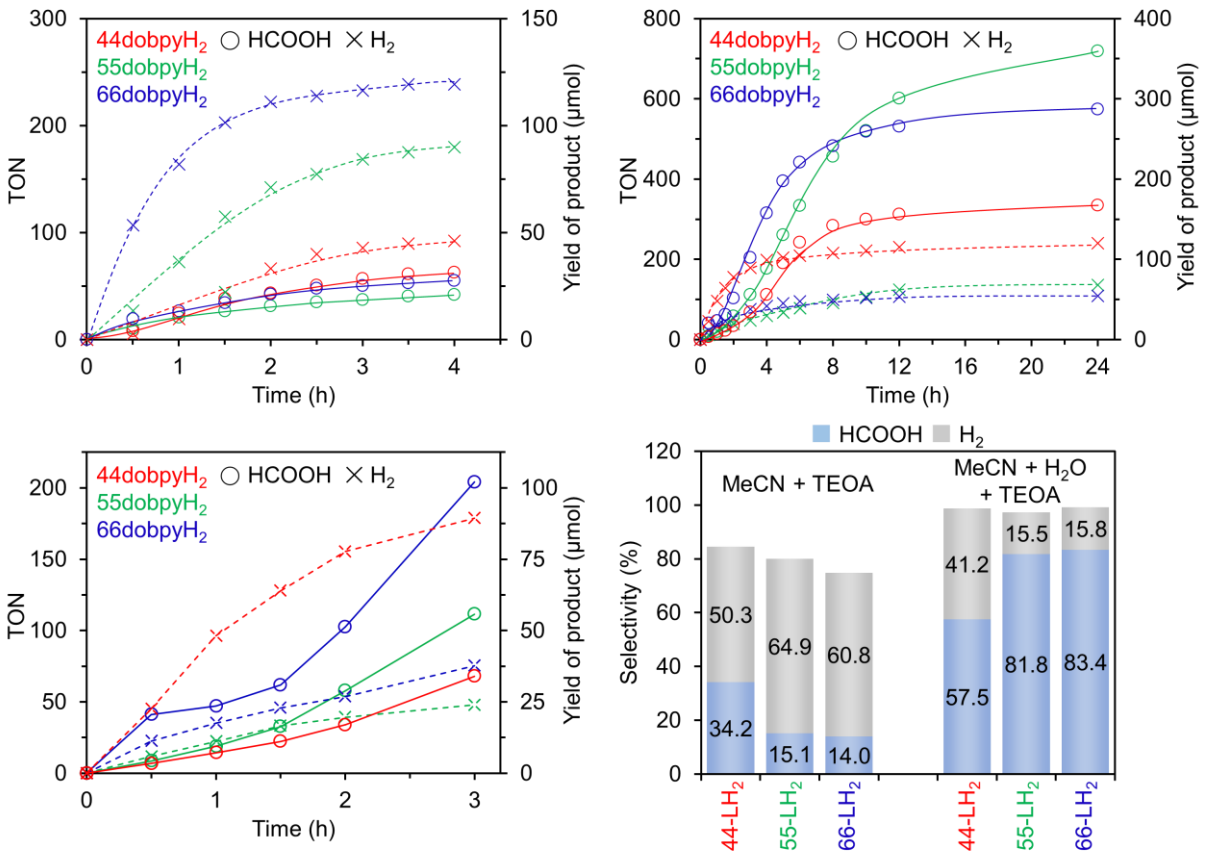

Figure 3. Photocatalytic CO_2 reduction into HCOOH and H_2 production for (a) CO_2-saturated MeCN+TEOA (5:1 v/v) and (b) CO_2-saturated MeCN+H_2O+TEOA (4:1:1 v/v) solutions containing $[Ru(bpy)_3]Cl_2$•$6H_2O$ (1.0 mM), BIH (0.1 M), and a **RhCp*(dobpyH$_2$)** derivative (0.1 mM) at 20 ºC under 300 W Xe lamp irradiation (λ > 400 nm). (c) Magnified view for the initial period in Figure 3b. (d) Summarized selectivity (%) in HCOOH and H_2 production. The CO production profiles are shown in Figure S11. Blank experiments without the catalyst are also shown in (Figure S12). Each measurement is repeated at least twice with an error margin of 1-15% to confirm the reproducibility.

https://doi.org/10.26434/chemrxiv-2024-t3ltd-v3 **ORCID:** https://orcid.org/0000-0003-4976-9796 Content not peer-reviewed by ChemRxiv. **License:** CC BY-NC-ND 4.0

electron donor under these conditions.[31,32] In the absence of water, the photocatalysis affords HCOOH and H_2 as the major products, where CO evolution is negligible in the initial stage but shows a gradual rise after the induction period of about 2 h (Figure S10), presumably due to unidentified alterations given in the coordination environments of catalytically active species at the prolonged reaction stage. For all catalysts, the H_2 production predominates over the HCOOH formation in the absence of water, as listed in Table 1 (entries 1-4) (see also Figures 3a,d and Figure S23). It must be noted that the H_2 evolution activity is the lowest for the non-hydroxylated **RhCp*(bpy)** catalyst (entry 1). To our great surprise, addition of water causes a complete switching in selectivity from H_2 into HCOOH only when catalyzed by the hydroxylated **RhCp*(dobpyH$_2$)** catalysts (Table 1, entries 6-8) (see also Figures 3b-d). Such a selectivity switching is not induced by the non-hydroxylated **RhCp*(bpy)** catalyst (Figure S23), indicative of the importance of having the hydroxyl functional groups to accelerate the formate formation in the presence of water. Moreover, the fundamental catalytic performances in terms of the total catalytic efficiency, defined by TON_{total}, increases substantially for all catalysts (Table 1). The reproducibility of our results has been successfully confirmed through three times of measurements for each condition. The highest catalytic performances in both the HCOOH yield (TON_{HCOOH}) and the HCOOH selectivity (Sel_{HCOOH}) are achieved by the **RhCp*(55dobpyH$_2$)** catalyst (TON_{HCOOH} = 720 and Sel_{HCOOH} = 82%). The **RhCp*(66dobpyH$_2$)** catalyst also shows an outstanding performance in HCOOH

Table 1. Summary of photocatalytic performances.[a]

Entry	Catalyst (0.1 mM)	Solvent	HCOOH		CO		H_2		TON_{total}[f]
			TON (μmol) [selectivity]	TOF_{max} (h^{-1})	TON (μmol) [selectivity]	TOF_{max} (h^{-1})	TON (μmol) [selectivity]	TOF_{max} (h^{-1})	
1[b]	**RhCp*(bpy)**	d	46 (23) [37%]	24	28 (14) [22%]	16	51 (26) [41%]	35	125
2[b]	**RhCp*(44dobpyH$_2$)**	d	63 (32) [34%]	33	28 (14) [15%]	2	92 (46) [50%]	54	183
3[b]	**RhCp*(55dobpyH$_2$)**	d	42 (21) [15%]	24	55 (28) [20%]	7	180 (90) [65%]	99	277
4[b]	**RhCp*(66dobpyH$_2$)**	d	55 (28) [14%]	39	99 (49) [25%]	16	239 (120) [61%]	254	393
5[c]	**RhCp*(bpy)**	e	146 (73) [40%]	41	37 (19) [10%]	7	183 (92) [50%]	74	366
6[c]	**RhCp*(44dobpyH$_2$)**	e	335 (167) [58%]	43	7 (3) [1%]	1	240 (120) [41%]	102	582
7[c]	**RhCp*(55dobpyH$_2$)**	e	720 (360) [82%]	83	23 (12) [2%]	5	136 (68) [16%]	24	879
8[c]	**RhCp*(66dobpyH$_2$)**	e	574 (287) [83%]	111	6 (3) [1%]	2	109 (55) [16%]	45	689

[a]The photocatalysis conditions are same to those shown in Figures 3a,b and S23. [b]TON at 4 h. [c]TON at 24 h. [d]MeCN/TEOA (5:1 v/v). [e]MeCN/H_2O/TEOA (4:1:1 v/v). [f]TON_{total} = TON_{HCOOH} + TON_{CO} + TON_{H2}.

https://doi.org/10.26434/chemrxiv-2024-t3ltd-v3 **ORCID:** https://orcid.org/0000-0003-4976-9796 Content not peer-reviewed by ChemRxiv. **License:** CC BY-NC-ND 4.0

production (TON_{HCOOH} = 574 and Sel_{HCOOH} = 83%). Meanwhile, the selectivity for H_2 evolution is significantly suppressed, in sharp contrast with the high activity and selectivity for H_2 in a water-free mixed solvent, except for the non-hydroxylated **RhCp*(bpy)** catalyst. To the best of our knowledge, this is the first report demonstrating the water-induced suppression in H_2 selectivity which concomitantly leads to the substantially enhanced formic acid production based on the introduction of hydroxyl groups into the bipyridyl ligand. Actually, it has been often reported that photocatalytic CO_2 reduction in such water-containing organic media tends to exhibit simultaneous increase in the yield of all reduction products (*i.e.*, HCOOH, CO and H_2) without showing any specific preference, [13,21d] as is the case for the **RhCp*(bpy)** catalyst examined as a control in this study. It seems also noteworthy that the photocatalytically active period is obviously prolonged by the presence of water.

The more careful examinations into all product formation profiles led us to focus on the following issues. First, it is important to pay attention to the fact that the **RhCp*(66dobpyH_2)** derivative which shows the highest activity in H_2 evolution in the absence of water exhibits the lowest yield in H_2 in the water-added system. Apparently, the two observations appear rather contradicting. Similarly, the **RhCp*(55dobpyH_2)** derivative shows a quite similar behavior. To the contrary, the **RhCp*(44dobpyH_2)** derivative, which shows the lowest activity in H_2 evolution in the absence of water, shows the earliest rise and the highest yield in H_2 evolution in the water-added system. In contrast, the **RhCp*(bpy)** shows no induction period in both products in the presence of water by showing obviously different characteristics compared to the hydroxylated catalysts (Figure S23). Secondly, we should also pay attention to the substantial difference in the induction period of HCOOH formation in the water-added system among the three catalysts (Figure 3c). The **RhCp*(44dobpyH_2)** shows the longest induction period as well as the lowest yield in HCOOH formation. Importantly, the **RhCp*(66dobpyH_2)** derivative shows almost no induction period, indicative of its high efficiency in the HCOOH formation. The **RhCp*(55dobpyH_2)** derivative also shows a relatively short induction period in HCOOH formation. Consequently, we hypothesized that, at least in the catalysis by the **RhCp*(66dobpyH_2)** and **RhCp*(55dobpyH_2)** derivatives, the H_2 once evolved in the water-added

https://doi.org/10.26434/chemrxiv-2024-t3ltd-v3 **ORCID:** https://orcid.org/0000-0003-4976-9796 Content not peer-reviewed by ChemRxiv. **License:** CC BY-NC-ND 4.0

system is effectively consumed in the CO_2 hydrogenation into HCOOH, since it well rationalizes the reason for the low yield in H_2 evolution by these catalysts. The validity of these arguments was experimentally confirmed, as described in the next section.

Chemical Speciation by Redox-dependent Proton Dissociation Constants

Since the photocatalysis was carried out in the presence of a large quantity of basic TEOA, dihydroxyl groups in $[Rh^{III}Cp^*(dobpyH_2)Cl]^+$ are expected to be partly or fully deprotonated in solution. As depicted in Scheme 3, three stepwise proton dissociation equilibria must be taken into consideration, as previously described.[26,33] Nevertheless, the metal-centered reductions as well as the bpy-based reduction certainly bring about non-negligible impacts to the pK_a values. The catalyst intermediates are thus considered to possess redox-dependent pK_a values. In general, successive reductions cause gradual increase in electron density at the bipyridyl moiety, leading to raise the pK_a values. The impact is expected to be significantly large upon the bpy-based reduction due to the direct injection of an electron into the bipyridyl moiety.

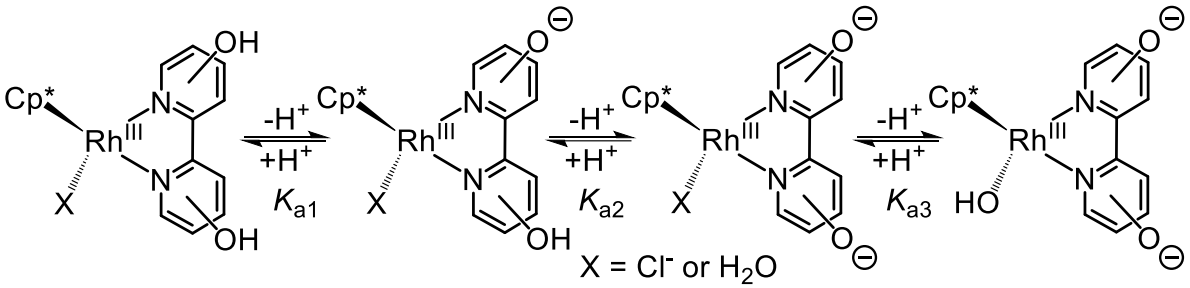

Scheme 3. Three possible proton dissociation equilibria supposed for $[Rh^{III}Cp^*(dobpyH_2)Cl]^+$.

To gain clearer insights into the protonation states of individual species, we adopted combination of experimental and theoretical approach described below. First, spectrophotometric pH titrations were carried out for all three catalysts in their initial $[Rh^{III}Cp^*(dobpyH_2)Cl]^+$ states. The global spectral analysis using the SVD (Singular Value Decomposition) method gave successful results, yielding the stepwise pK_a values together with the molar absorptivity spectra of individual species (Figures S25-

https://doi.org/10.26434/chemrxiv-2024-t3ltd-v3 **ORCID:** https://orcid.org/0000-0003-4976-9796 Content not peer-reviewed by ChemRxiv. **License:** CC BY-NC-ND 4.0

S29). Over the pH range of 2-9, the $[Rh^{III}Cp^*(44dobpyH_2)Cl]^+$ and $[Rh^{III}Cp^*(55dobpyH_2)Cl]^+$ derivatives show two-step proton dissociation equilibria, while only the $[Rh^{III}Cp^*(66dobpyH_2)Cl]^+$ derivative shows three-step equilibria (pK_{a3} = 8.21(9); see Figure S27). The experimentally determined pK_{a1} and pK_{a2} values for these $[Rh^{III}Cp^*(dobpyH_2)Cl]^+$ catalysts are listed in Table 2, together with the pK_a values calculated for several relevant species in different redox or protonation states. For each ligand system, the observed and calculated pK_{a2} values for the $[Rh^{III}Cp^*(dobpyH_2)Cl]^+$ catalyst show a

Table 2. Observed and calculated pK_a values for the **RhCp*(dobpyH₂)** derivatives in various forms.[a]

Protonated Species Computed by DFT	**RhCp*(44dobpyH₂)**		**RhCp*(55dobpyH₂)**		**RhCp*(66dobpyH₂)**	
	pK_{a1} (Obsd.)	pK_{a2} (Obsd.)	pK_{a1} (Obsd.)	pK_{a2} (Obsd.)	pK_{a1} (Obsd.)	pK_{a2} (Obsd.)
$^1[Rh^{III}Cp^*(dobpyH_2)Cl]^+$	4.87[b] (4.87)	5.50 (6.12)	5.64[b] (5.64)	6.81 (6.89)	4.84[b] (4.84)	6.11 (5.97)
$^1[Rh^{I}Cp^*(dobpyH_2)]$	7.55	9.25	9.29	10.28	9.12	9.39
$^2[Rh^{I}Cp^*(dobpyH_2^{-\bullet})]^-$	12.80	13.17	13.92	22.28	14.49	15.53
$^1[Rh^{III}(H)Cp^*(dobpyH_2)]^+$	3.42	4.35	5.43	7.45	5.01	6.16
$^2[Rh^{III}(H)Cp^*(dobpyH_2^{-\bullet})]$	11.11	14.45	5.52	9.86	10.12	13.00

[a]Computed using the CAM-B3LYP/SDD(Rh)/6-311+G*(others) level of DFT with the solvation model based on the density (SMD, water). [b]The values are benchmarked using the experimentally determined pK_{a1} values.

good consistency, demonstrating the validity of the calculation method adopted (see Experimental Section). The results of calculations allow us to understand several tendencies as follows. (i) The Rh^{III}/Rh^{I} reduction (*i.e.*, 2-electron reduction) results in increase in all pK_a values by about 3~4 units. (ii) The $Rh^{III}(LH_2)$/ $Rh^{I}(LH_2^{-\bullet})$ reduction (*i.e.*, 3-electron reduction) leads to the substantial increase in pK_a by at least *ca.* 8 units. (iii) The protonation of Rh^{I} to give $Rh^{III}(H)$ generally causes decrease in electron density at the bipyridyl moiety leading to show a decrease in pK_a, where the non-bpy-reduced species show a decrease in pK_a by 3~5 units while the bpy-reduced species exhibit irregular behaviors. (iv) The bpy-reduced derivatives possess relatively high pK_a values. These tendencies are quite useful in order to rationally select the most abundant form of each intermediate when we make approach to the mechanistic interpretations below.

We also note that the deprotonated pyridyl rings all similarly bear a double bond character at the C-

https://doi.org/10.26434/chemrxiv-2024-t3ltd-v3 **ORCID:** https://orcid.org/0000-0003-4976-9796 Content not peer-reviewed by ChemRxiv. **License:** CC BY-NC-ND 4.0

O bond (ca. 1.25 Å) without losing the aromaticity in the pyridyl donor regardless of the substituent positions, indicative of the preservation of d(Rh)-π*(bpy) associations (Figures S32-S34). In other words, the amido character, expected for the keto tautomer by the 4,4'- and 6,6'-substituted catalysts, is not evident at the nitrogen donor in the deprotonated rings. Nevertheless, we note that the experimentally determined pK_a values of $[Rh^{III}Cp^*(44dobpyH_2)Cl]^+$ and $[Rh^{III}Cp^*(66dobpyH_2)Cl]^+$ are by 1 unit lower than the corresponding values of $[Rh^{III}Cp^*(55dobpyH_2)Cl]^+$, indicative of the higher stabilization of the deprotonated species for the former two catalysts compared to the latter. These observations seem reflecting the non-negligible impacts arising from the difference in the resonance forms between the ortho-para and the meta substituted bipyridyl ligands.

Carbon Dioxide Hydrogenation Slowly Catalyzed in the Dark

To confirm the role of H_2-consumption pathway supposed to accelerate the overall photocatalytic HCOOH formation, hydrogenation of CO_2 in the dark catalyzed by the **RhCp*(dobpyH$_2$)** derivatives, together with the **RhCp*(bpy)** derivative, were investigated. First, an aqueous $NaHCO_3$ buffer solution containing each catalyst (pH 8.3) was purged with a 1:1 H_2/CO_2 syngas (1 atm) to determine the HCOOH formation yield. Obviously, the doubly deprotonated species $[Rh^{III}Cp^*(dobpy)Cl]^-$ is regarded

Table 3. CO_2 hydrogenation performances.[a]

Complex	HCOOH	
	TON	μmol
RhCp*(bpy)	n.d.	n.d.
RhCp*(44dobpy)	52	26
RhCp*(55dobpy)	77	38
RhCp*(66dobpy)	95	47

[a]Catalysis conditions: The reaction is carried out in an aqueous $NaHCO_3$ (1.0 M, pH 8.3) solution of a rhodium complex (0.1 mM) under the 1 atm syngas (H_2/CO_2 = 1:1, v/v) condition for 24 h at 20 ºC. Blank experiment without the catalyst does not generate HCOOH.

https://doi.org/10.26434/chemrxiv-2024-t3ltd-v3 **ORCID:** https://orcid.org/0000-0003-4976-9796 Content not peer-reviewed by ChemRxiv. **License:** CC BY-NC-ND 4.0

as the major species at pH 8.3 (pK_{a2} < 7 for all catalysts; see Table 2). As summarized in Table 3, the **RhCp*(66dobpyH$_2$)**, showing almost no induction period in photocatalytic HCOOH formation in the water-added system (Figure 3b), exhibits the highest HCOOH formation activity (TON_{HCOOH} = 95), whereas the **RhCp*(44dobpyH$_2$)**, showing the longest induction period in HCOOH formation in Figure 3b, exhibits the lowest activity (TON_{HCOOH} = 52). It is important to focus on the fact that no HCOOH forms when the non-hydroxylated **RhCp*(bpy)** is adopted, revealing the importance of hydroxyl groups to promote the catalytic hydrogenation**.** We have also confirmed that the CO_2 hydrogenation by these catalysts is not accelerated by visible light irradiation in the absence of RuPS and BIH (data not shown). These results demonstrate that the HCOOH formation *via* the dark hydrogenation catalyzed by the **RhCp*(dobpyH$_2$)** derivatives indeed proceeds. However, the observed rates are clearly much lower than those observed in the photocatalytic reactions, which is partly attributable to the inability to promote further reduction of the $[Rh^{III}(H)Cp^*(dobpy)]^-$ into the bpy-reduced $Rh^{III}(H)Cp^*(dobpyH_2^{-\bullet})$ due to the lack of $RuPS^{-\bullet}$, as illustrated in Scheme 4. Thus, the dark hydrogenation cannot make access to the bpy-reduced intermediate $Rh^{III}(H)Cp^*(LH_2^{-\bullet})$ so that the slow path is only available. In other words, the bpy-reduced species is the actual key intermediate attacking CO_2 to yield formate in a faster photocatalytic route, as described below in the DFT section. We also note that $[Rh^{III}Cp^*(dobpy)Cl]^-$ preserves its ligation by chloride in solution (Figure S28) and requires the substitution of Cl^- with H_2 to trigger the hydride formation, which also rationalizes the sluggishness of the dark reactions (see below).

In order to further ascertain whether the dark hydrogenation indeed proceeds under the photocatalytic conditions, the photocatalysis solutions themselves were adopted to monitor the H_2-consumption-based HCOOH formation (Figure S24). Using the molar absorptivity spectra determined in the pH titration experiments (Figure S29), the major species appearing after the dissolution of each catalyst was also judged to be the doubly deprotonated species $[Rh^{III}Cp^*(dobpy)Cl]^-$ (Figure S31). In these additional experiments, the photocatalysis described above for Figure 3b was similarly conducted until the induction period is completed, followed by purging the solution with a H_2/CO_2 gas mixture having a mixing ratio of either 5:5 or 1:9. Even with the observed slow rates in HCOOH formation, the

https://doi.org/10.26434/chemrxiv-2024-t3ltd-v3 **ORCID:** https://orcid.org/0000-0003-4976-9796 Content not peer-reviewed by ChemRxiv. **License:** CC BY-NC-ND 4.0

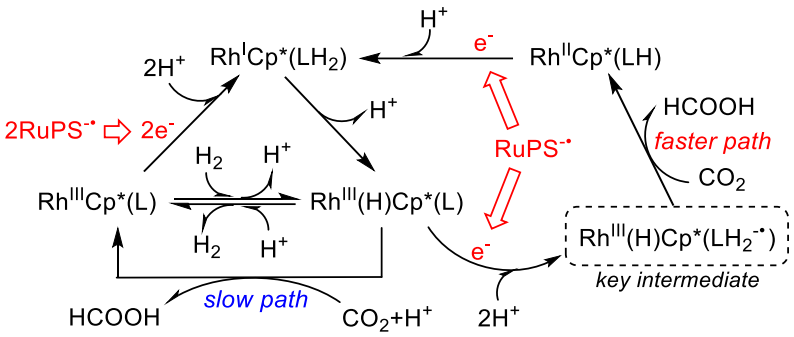

Scheme 4. Multiple pathways in competition in the photocatalysis. The protonation states of species obey the pK_a values in Table 2, except for the assumption on $Rh^{II}Cp^*(LH)$.

results further demonstrate that the "slow hydrogenation path" is also active under the photocatalytic conditions. We can therefore consider that the rhodium hydride crucial for producing HCOOH[34] during the photocatalysis can be given not only *via* the photocatalytic 3-electron reductions of the Rh^{III} species by $RuPS^{-\bullet}$ but also *via* the simple H_2 addition to the Rh^{III} species with additional 1-electron reduction by $RuPS^{-\bullet}$ (Scheme 4). The induction periods seen in the photocatalytic HCOOH formation by the **RhCp*(55dobpyH$_2$)** and **RhCp*(44dobpyH$_2$)** derivatives in Figure 3b may be correlated with the time required to establish the so-called stationary conditions in promoting such competitively promoted photocatalytic and non-photocatalytic processes.

https://doi.org/10.26434/chemrxiv-2024-t3ltd-v3 **ORCID:** https://orcid.org/0000-0003-4976-9796 Content not peer-reviewed by ChemRxiv. **License:** CC BY-NC-ND 4.0

To elucidate the observed differences in the catalytic activity towards the dark CO_2 hydrogenation, the H_2 addition to the individual catalyst was studied by DFT calculations. Figure 4 shows the DFT results on the reaction of H_2 with the doubly deprotonated $Rh^{III}Cp^*$(66dobpy), considered as the major species in solution (see above). The initial intermediate can be supposed as a dihydrogen complex $Rh^{III}(H_2)Cp^*$(66dobpy). For all catalysts, a similar dihydrogen intermediate can be supposed, as

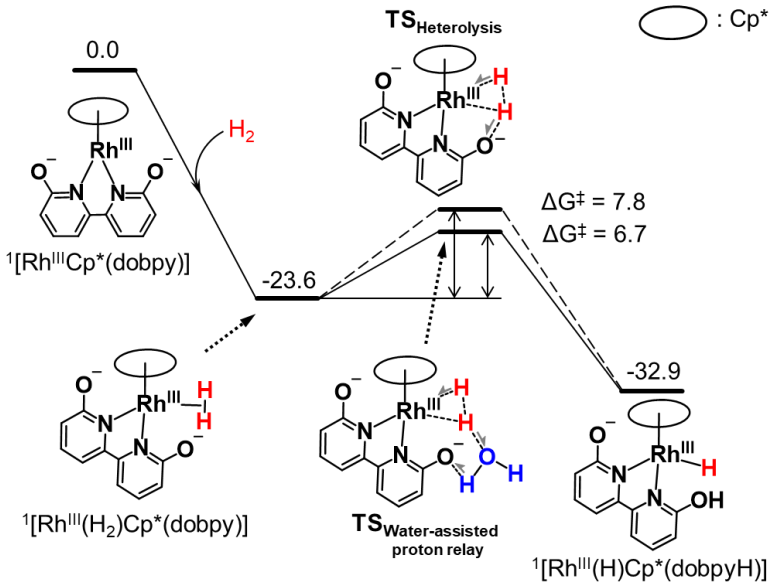

Figure 4. The Gibbs free energy diagram computed by DFT for the H_2 heterolysis by the **RhCp*(66dobpy)** catalyst. Each value is in kcal/mol. All the structures have been optimized at the M06/SDD(Rh)/ 6-31G*(others) level of DFT with solvation in acetonitrile taken into consideration (C-PCM).

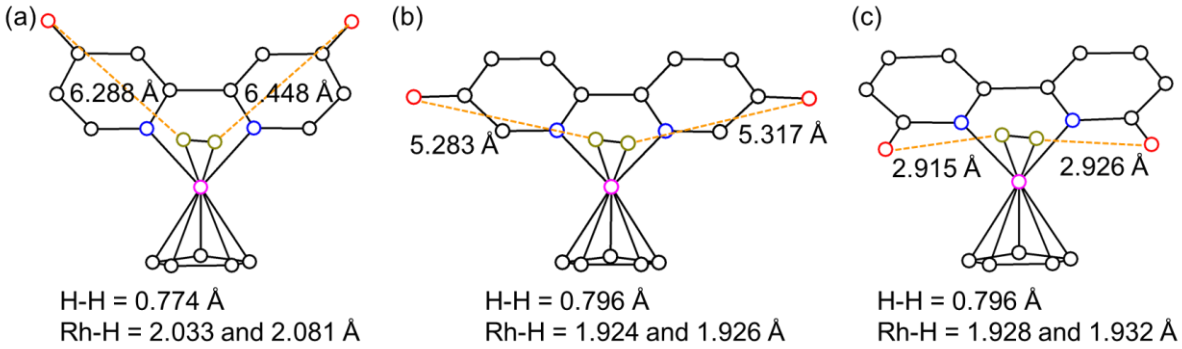

Figure 5. DFT-optimized structures of singly deprotonated catalysts ligated by H_2: (a) $Rh^{III}(H_2)Cp^*$(44dobpy), (b) $Rh^{III}(H_2)Cp^*$(55dobpy), and (c) $Rh^{III}(H_2)Cp^*$(66dobpy), where methyl groups on the Cp* and hydrogens on the bpy moieties have been omitted for clarity.

https://doi.org/10.26434/chemrxiv-2024-t3ltd-v3 **ORCID:** https://orcid.org/0000-0003-4976-9796 Content not peer-reviewed by ChemRxiv. **License:** CC BY-NC-ND 4.0

depicted in Figure 5. The H-H distances in these dihydrogen complexes are in the range of 0.774-0.796 Å, only slightly longer than that of free H_2 (0.742 Å, computed using the same level of calculations) and thereby represent them as nearly pure σ-complexes with a smaller contribution of π-back donation to the H-H antibonding orbital, *i.e.*, σ*(1s-1s).[35]

An intriguing discovery in our DFT calculations is that the dihydrogen complex $Rh^{III}(H_2)$Cp*(66dobpy) can feasibly overcome the barrier ($\Delta G^{\ddagger}$ = 7.8 kcal/mol) to afford a hydride intermediate, *i.e.*, Rh^{III}(H)Cp*(66dobpyH), as a result of heterolytic cleavage of H_2 into a hydride and a proton with concomitant transfer of the proton to make one of the oxo groups protonated (Figure 4). Overall, this step is an exothermic process ($\Delta G_{cleavage}$ = -9.3 kcal/mol). In order to fully understand the detailed structural changes during the heterolytic H-H cleavage, we further conducted the intrinsic reaction coordinate (IRC) calculation for this step (Figure S13). While passing through the transition state (TS), one of the H atoms is withdrawn by the basic oxo site (O-H = 1.400 Å at TS) and the H-H bond distance becomes longer (H-H = 0.960 Å at TS). At the same time, the other H atom becomes closer to the Rh center (Rh-H = 1.802 Å). In addition to this pathway (*i.e.*, direct H-H cleavage pathway), a water-assisted pathway showing a slightly lower barrier ($\Delta G^{\ddagger}$ = 6.7 kcal/mol) was also realized (see Figure 4), which has a strong relevance to the behaviors described for the IrCp* analogs.[27b] Although we have been unsuccessful in determining the TS energies for the rest of catalysts, their H_2 cleavage steps are similarly downhill in nature (Table S1). The values of $\Delta G_{cleavage}$ = -17.6 and -23.6 kcal/mol were obtained for $Rh^{III}(H_2)$Cp*(44dobpy) and $Rh^{III}(H_2)$Cp*(55dobpy), respectively. It seems likely that they can also promote the heterolytic cleavage *via* the water-accelerated pathways.

It is also important to discuss the interatomic distances between the protons and the oxo oxygens which may play a role as a proton relay site to accelerate the heterolytic cleavage of H_2.[36] This issue can be viewed as related to the role of pendant amine sites known to enhance the catalytic activity of hydrogenase enzymes and their artificial models.[37] As illustrated in Figure 5, the $H(H_2)$-O(oxo) distances for $Rh^{III}(H_2)$Cp*(44dobpy) and $Rh^{III}(H_2)$Cp*(55dobpy) are substantially longer than that for $Rh^{III}(H_2)$Cp*(66dobpy), rationalizing the reason why the TS optimization for the H_2 cleavage within

https://doi.org/10.26434/chemrxiv-2024-t3ltd-v3 **ORCID:** https://orcid.org/0000-0003-4976-9796 Content not peer-reviewed by ChemRxiv. **License:** CC BY-NC-ND 4.0

$Rh^{III}(H_2)Cp^*$(44dobpy) and $Rh^{III}(H_2)Cp^*$(55dobpy) is not straightforward. Nevertheless, our experiments also evidenced that the **RhCp*(bpy)**, having no hydroxyl groups, does not catalyze the CO_2 hydrogenation to HCOOH under the same reaction conditions (Table 3). The results clearly indicate that the oxo oxygens at the remote sites in these catalysts indeed play a significant role in the H_2 cleavage to promote the dark CO_2 hydrogenation. These results strongly suggest that the CO_2 hydrogenation catalyzed by these $Rh^{III}Cp^*$(dobpy) derivatives is all likely promoted *via* the water-accelerated pathways using the oxo as a proton relay site.

Stability of Catalysts

To verify the stability of our photocatalytic systems, the electrospray ionization mass spectrometry (ESI-MS) was used to observe the molecular species in solution before and after the photolysis. With this purpose, the photocatalysis condition adopted for entry 7 in Table 1, which shows the highest photocatalytic performance, was adopted. The measurements were carried out for the cationic species deposited by adding an excess of sodium tetraphenylborate to the photocatalysis solution. As shown in Figure 6, the mass patterns observed for the species deposited before and after the photocatalysis are fundamentally identical, revealing that the cationic species are all well intact during at least the initial 2.5 h of photocatalysis. The results evidence that the induction period is attributable to neither the transformation nor decomposition of any species including the **RhCp*(55dobpyH$_2$)** catalyst. The four cationic species observed are unambiguously assigned as $[BI]^+$, $[BIH{\cdot}H_2O]^+$, $[Ru(bpy)_3]^{2+}$, and $[Rh^{III}Cp^*(55dobpyH)(R_2NH\text{-}CH_2CH_2\text{-}OCO_2)]^+$, where $R_2NH\text{-}CH_2CH_2\text{-}OCO_2$ (R=CH_2CH_2OH) is a zwitterion (*i.e.*, $R_2N^+H\text{-}CH_2CH_2\text{-}OCO_2^-$) given as a covalent bonding of CO_2 and TEOA, as described elsewhere.[31b,c] It should be noted that the $R_2NH\text{-}CH_2CH_2\text{-}OCO_2$ ligand can remain coordinated while the metal has an oxidation state of Rh^{III}. Our DFT calculations clearly reveal that the Rh^{III}-O($R_2NH\text{-}CH_2CH_2\text{-}OCO_2$) bond can only be stabilized with the distance being 2.17 Å, while those for the Rh^{II} and Rh^{I} catalysts are entirely dissociated into 3.86 and 4.07 Å, respectively (Figure S15). These reflect

https://doi.org/10.26434/chemrxiv-2024-t3ltd-v3 **ORCID:** https://orcid.org/0000-0003-4976-9796 Content not peer-reviewed by ChemRxiv. **License:** CC BY-NC-ND 4.0

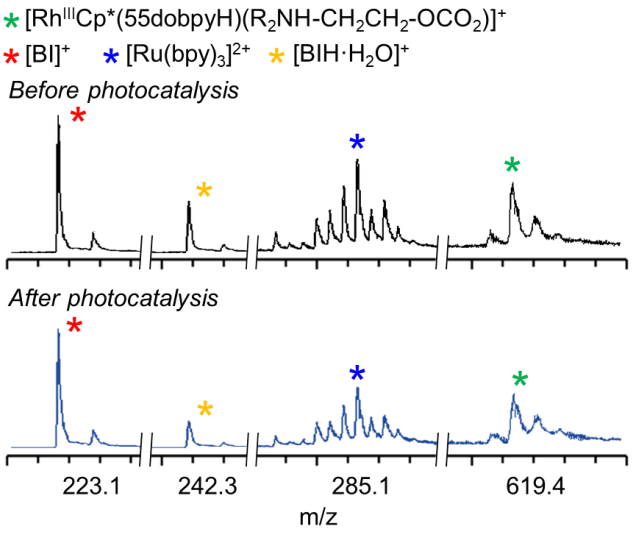

Figure 6. ESI-MS spectra observed for the cationic species deposited before and after 2.5 h of photolysis, where the conditions used for entry 7 in Table 1 was adopted. The cationic species in solution were once precipitated as by adding a large excess of $NaBPh_4$ followed by dissolving the solid sample in acetonitrile to measure the spectra (see Figure S14 for more details).

the Jahn-Teller distortion in the low-spin d^7 Rh^{II} center as well as the pseudo-square-planar geometry established by the d^8 Rh^{I} center. We also note that the $R_2N^+H\text{-}CH_2CH_2\text{-}OCO_2^-$ ion does not itself participate in the catalysis of CO_2 reduction, since the carbon center of CO_2 in this adduct has a poor electrophilicity and cannot be the target of nucleophilic attack by either a metal or a metal-hydride.

On the other hand, the results of photocatalytic CO_2-to-HCOOH conversion in the water-added mixture indicate that **RhCp*(66dobpyH$_2$)** exhibits the highest maximum TOF (*i.e.*, TOF_{max}), whereas **RhCp*(55dobpyH$_2$)** demonstrates the highest TON_{HCOOH} (Table 1). The higher TON_{HCOOH} value (720) achieved by **RhCp*(55dobpyH$_2$)** relative to **RhCp*(66dobpyH$_2$)** (TON_{HCOOH} = 574) seems like reflecting its higher stability. These features can be well recognized by the crossing of the HCOOH formation profiles of these catalysts at 8 h, together with the induction period only seen for **RhCp*(55dobpyH$_2$)** (Figure 3b). In spite of the superior catalytic rate of the **RhCp*(66dobpyH$_2$)** derivative, this catalyst is found to be rather inferior in its stability during the photocatalysis. Two possible reasons can be pointed out as follows. First, the **RhCp*(66dobpyH$_2$)** derivative possesses an intense as well as broad visible absorption band above 400 nm, which is not seen for other catalysts

https://doi.org/10.26434/chemrxiv-2024-t3ltd-v3 **ORCID:** https://orcid.org/0000-0003-4976-9796 Content not peer-reviewed by ChemRxiv. **License:** CC BY-NC-ND 4.0

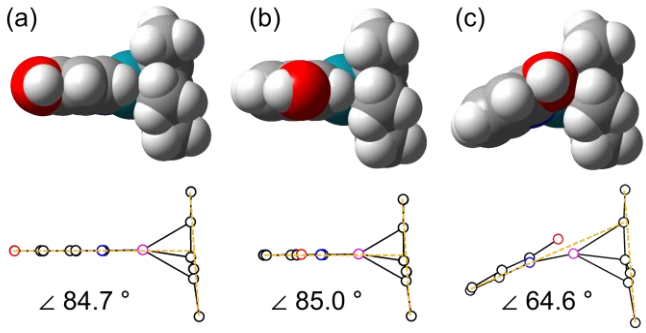

Figure 7. Dihedral angles between the $dobpyH_2$ and Cp* planes for (a) ^{1}[Rh^{I}Cp*(44$dobpyH_2$)], (b) ^{1}[Rh^{I}Cp*(55$dobpyH_2$)], and (c) ^{1}[Rh^{I}Cp*(66$dobpyH_2$)].

(Figure S16). It is therefore quite reasonable to consider that the photodegradation of this catalyst is much more severely enhanced compared to other catalysts. Second, through our DFT studies, we encountered the fact that somewhat unusual structural strain is only established in the **RhCp*(66dobpyH$_2$)** species due to the intramolecularly established steric hindrances by the 6,6'-hydroxyl groups on the $dobpyH_2$ ligand. As depicted in Figure 7, an exceptional canting of the $dobpyH_2$ plane with regard to the Cp* plane is given only by the **RhCp*(66dobpyH$_2$)** catalyst, indicative of the difficulty in forming an ideal coordination mode of the bpy chelate which are achievable by the 44$dobpyH_2$ and 55$dobpyH_2$ moieties. Here the hydride intermediates with 1-electron reduced at the $dobpyH_2$ moiety (*i.e.*, ^{2}[Rh^{III}(H)Cp*($dobpyH_2^{\bullet-}$)]) are adopted to compare the structural features since they are judged to serve as a key intermediate in HCOOH formation (see below). This factor is likely to contribute to the relatively lower stability of the **RhCp*(66dobpyH$_2$)** catalyst.

Mechanistic Studies

To elucidate the mechanism of formate generation in the photochemical CO_2 reduction catalyzed by the **RhCp*(dobpyH$_2$)** derivatives, DFT calculations were carried out to develop the free energy diagrams showing possible reaction pathways (Figure 8 and Table S2). For the simplicity, the non-deprotonated form of the ligand ($dobpyH_2$) is adopted to model the possible reaction pathways, considering the

https://doi.org/10.26434/chemrxiv-2024-t3ltd-v3 **ORCID:** https://orcid.org/0000-0003-4976-9796 Content not peer-reviewed by ChemRxiv. **License:** CC BY-NC-ND 4.0

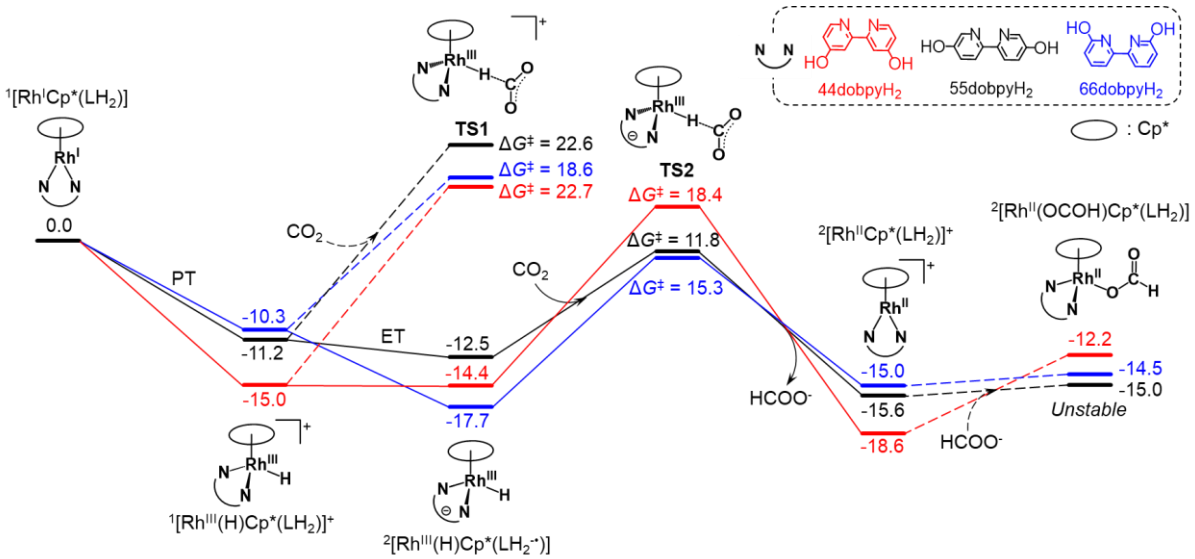

Figure 8. The Gibbs free energy diagram computed by DFT for the CO_2 reduction to formate catalyzed by the **RhCp*(dobpyH$_2$)** derivatives when driven by the reductive equivalent based on the $[Ru(bpy)_3]^{2+}/[Ru(bpy)_2(bpy^{\bullet-})]^+$ couple (-1.76 V vs. Fc/Fc^+ in MeCN) with the protonation step promoted by $[TEOA(H)]^+$ (pK_a = 15.9) as a proton source. Each value is given in kcal/mol.

relatively high pK_a values for the lower redox intermediates appearing in the diagrams (Table 2). To ensure the consistency with the conditions adopted for the photocatalytic reactions, the reduction potential of $[Ru(bpy)_3]^{2+}/[Ru(bpy)_2(bpy^{\bullet-})]^+$ (-1.76 V vs. Fc/Fc^+ in MeCN) [29,30] was used to estimate the driving force for each electron transfer step. Similarly, the value of pK_a = 15.9 reported for $[TEOA(H)]^+$ was adopted to benchmark the protonation processes.[32] The validity of our treatments was also confirmed by comparing the computed potentials for either the $Rh^{III/II}$ or $Rh^{II/I}$ couple with those experimentally determined by the SWV.

In Figure 8, the major reaction pathways are illustrated in black lines using those computed for the **RhCp*(55dobpyH$_2$)** derivative with the corresponding pathways for the **RhCp*(44dobpyH$_2$)** and **RhCp*(66dobpyH$_2$)** derivatives also shown in red and blue, respectively. The following arguments mainly use the pathways derived from the **RhCp*(55dobpyH$_2$)** derivative. The diagram starts with ^{1}[Rh^{I}Cp*(LH$_2$)], with the chloride in the initial species dissociated upon 2-electron reduction.[28] The thermodynamic stability of this species was unambiguously confirmed by conducting additional calculations (Figure S17). Protonation of this species leading to afford Rh^{III}(H), *i.e.*, ^{1}[Rh^{III}(H)Cp*(dobpyH$_2$)]$^+$, is thermodynamically feasible as a subsequent step.[38] Although Figure 8 was

https://doi.org/10.26434/chemrxiv-2024-t3ltd-v3 **ORCID:** https://orcid.org/0000-0003-4976-9796 Content not peer-reviewed by ChemRxiv. **License:** CC BY-NC-ND 4.0

originally constructed by ignoring the redistribution in the proton dissociation equilibria, the detailed pK_a properties obtained at the revision stage (Table 2) clearly indicated the complete deprotonation of Rh^{III}(H) to yield $^1[Rh^{III}(H)Cp^*(dobpy)]^-$ as a major species. We therefore had to re-examine whether the PT-ET pathway for the induvial catalyst is indeed feasible through the fully deprotonated Rh^{III}(H) species. The PT-ET pathways through all three possible protonation states are illustrated in Figures S35-S37. The results reveal that the ET step through $^1[Rh^{III}(H)Cp^*(dobpy)]^-$ to yield $^2[Rh^{III}(H)Cp^*(dobpyH_2^{-\bullet})]$ is similarly feasible for the 5,5'- and 6,6'-substituted catalysts but becomes endergonic (ΔG = 10 kcal/mol) for the 4,4'-substituted catalyst. Interestingly, this finding is rather consistent with the relatively slow photocatalytic reaction exhibited by the 4,4'-substituted catalyst. We additionally note that the contribution of a CPET (concerted proton-electron transfer) route to yield $^2[Rh^{III}(H)Cp^*(dobpyH_2^{-\bullet})]$ from $^1[Rh^{I}Cp^*(dobpyH_2)]$ without ligand deprotonation cannot be ruled out.

A possibility of affording Cp*-protonated intermediates, e.g., $[Rh^{I}(Cp^*H)(bpy)]^+$, was reported in the literature.[39] However, we will not discuss the pathways arising from such species, although we have also confirmed the feasibility of catalytic paths for formate formation using such Cp*-protonated intermediates (Figure S18). On the other hand, the CO_2 binding to $^1[Rh^{I}Cp^*(LH_2)]$, often crucial for the CO production, is rather considered to be disfavored (ΔG = 7.9~8.8 kcal/mol, $\Delta G^{\ddagger}$ not determined) (Figure S19). The combined results reveal that the protonation of $^1[Rh^{I}Cp^*(LH_2)]$ affording $^1[Rh^{III}(H)Cp^*(LH_2)]^+$ is the most favorable path to promote. It must be noted that this step is promotable due to the presence of $[TEOA(H)]^+$ but is not favored under the electrocatalytic conditions shown in Figure 1. Although we examined the availability of the formate formation *via* hydride transfer[40] using $^1[Rh^{III}(H)Cp^*(LH_2)]^+$, the activation barrier for producing formate from this species is rather demanding ($\Delta G^{\ddagger}$ = 22.6 kcal/mol) (see **TS1** in Figure 8). Moreover, both **RhCp*(44dobpyH$_2$)** and **RhCp*(66dobpyH$_2$)** similarly show a relatively high barrier by showing $\Delta G^{\ddagger}$ = 22.7 and 18.6 kcal/mol, respectively. We have also confirmed that these tendencies remain unchanged even if one of the hydroxyl groups is deprotonated (Figure S20).

We then evaluated the thermodynamic hydricity (ΔG_{H^-}) of $^1[Rh^{III}(H)Cp^*(L)]^-$ to understand their

https://doi.org/10.26434/chemrxiv-2024-t3ltd-v3 **ORCID:** https://orcid.org/0000-0003-4976-9796 Content not peer-reviewed by ChemRxiv. **License:** CC BY-NC-ND 4.0

efficiency in hydride transfer. As supplied in Table S4, we computed the ΔG_{H^-} values for all the protonation states using the two different levels of DFT with different solvation conditions, *i.e.*, M06/C-PCM(MeCN) and CAM-B3LYP/SMD(water). In both calculation models, the hydricity is found to be highly dependent on the protonation state by showing stepwise decrease in ΔG_{H^-} by successive deprotonation. The ΔG_{H^-} values for $^1[Rh^{III}(H)Cp^*(L)]^-$ in MeCN (C-PCM) were found to be 62.7, 72.6, and 64.7 kcal/mol for the 4,4'-, 5,5'-, and 6,6'-subsituted catalysts, respectively. These values are significantly higher than the 44.2-kcal/mol threshold required for the generation of $HCOO^-$ in MeCN,[34,41] indicating that these $^1[Rh^{III}(H)Cp^*(L)]^-$ intermediates possess an extremely low efficiency in hydride transfer. As an additional clue, the results using the CAM-B3LYP/SMD(water) model provide quite similar behaviors (Table S4). Such intriguing pH-dependent tunability in hydricity has never been discussed in the literature and can be utilized as a new strategy to control various types hydride transfer reactions of interest.

It is also noteworthy that the $^1[Rh^{III}(H)Cp^*(LH_2)]^+$ species similarly cannot evolve H_2 *via* the proton transfer from $[TEOA(H)]^+$ (pK_a = 15.9), since the hydricity must be lower than the 55-kcal/mol threshold required for the H_2 evolution under these conditions, as reported elsewhere.[42] We therefore pay attention to the hydride transfer *via* the bpy-reduced intermediate, *i.e.*, $^2[Rh^{III}(H)Cp^*(LH_2^{-\bullet})]$, which is energetically accessible by all the **RhCp*(dobpyH$_2$)** derivatives (ΔG = -7.4 ~ 0.6 kcal/mol). The spin density computed for these species clearly shows the delocalization of the unpaired electron over the dobpyH_2 ligand (Figure S21). As shown in Figure 8, the **RhCp*(55dobpyH$_2$)** derivative can undertake hydride transfer to CO_2 to afford $HCOO^-$ with a relatively low activation barrier of $\Delta G^{\ddagger}$ = 11.8 kcal/mol (**TS2**). The suppression in the **TS2** barrier presumably results from the increased electron density at the Rh^{III}-H center due to the higher donating strength by the 1-electron-reduced dobpyH_2 donors (Figure S22). The **TS2** barrier for the **RhCp*(66dobpyH$_2$)** derivative also shows a feasibility of this step ($\Delta G^{\ddagger}$ = 15.3 kcal/mol), while that for the **RhCp*(44dobpyH$_2$)** derivative is rather higher compared with other catalysts ($\Delta G^{\ddagger}$ = 18.4 kcal/mol). These results well agree with the observed tendency in the rate of photocatalytic HCOOH formation shown in Figure 5. The feasibility of these hydride transfer steps can

https://doi.org/10.26434/chemrxiv-2024-t3ltd-v3 **ORCID:** https://orcid.org/0000-0003-4976-9796 Content not peer-reviewed by ChemRxiv. **License:** CC BY-NC-ND 4.0

also be convinced by the substantially increased hydricity of $^{2}[Rh^{III}(H)Cp^{*}(LH_{2}^{-\bullet})]$. The ΔG_{H^-} values computed by the M06/C-PCM(MeCN) model are 43.4, 40.4 and 47.0 kcal/mol for the 4,4'-, 5,5'-, and 6,6'-subsituted catalysts, respectively. These values more or less satisfy the 44.2-kcal/mol threshold to promote the hydride transfer to CO_2. Our DFT results using the CAM-B3LYP/SMD(water) model also unveil the substantial increase in hydricity (*i.e.*, decrease in ΔG_{H^-}) upon deprotonation of this intermediate (Table S4). The much higher initial photocatalytic rate for the **RhCp*(66dobpyH₂)** derivative relative to the **RhCp*(55dobpyH₂)** derivative is likely relevant to the higher driving force for the ET from $[Ru(bpy)_2(bpy^{-\bullet})]^{+}$ to $^{1}[Rh^{III}(H)Cp^{*}(LH_2)]^{+}$ leading to yield $^{2}[Rh^{III}(H)Cp^{*}(LH_{2}^{-\bullet})]$ (ΔG = -7.4 kcal/mol).

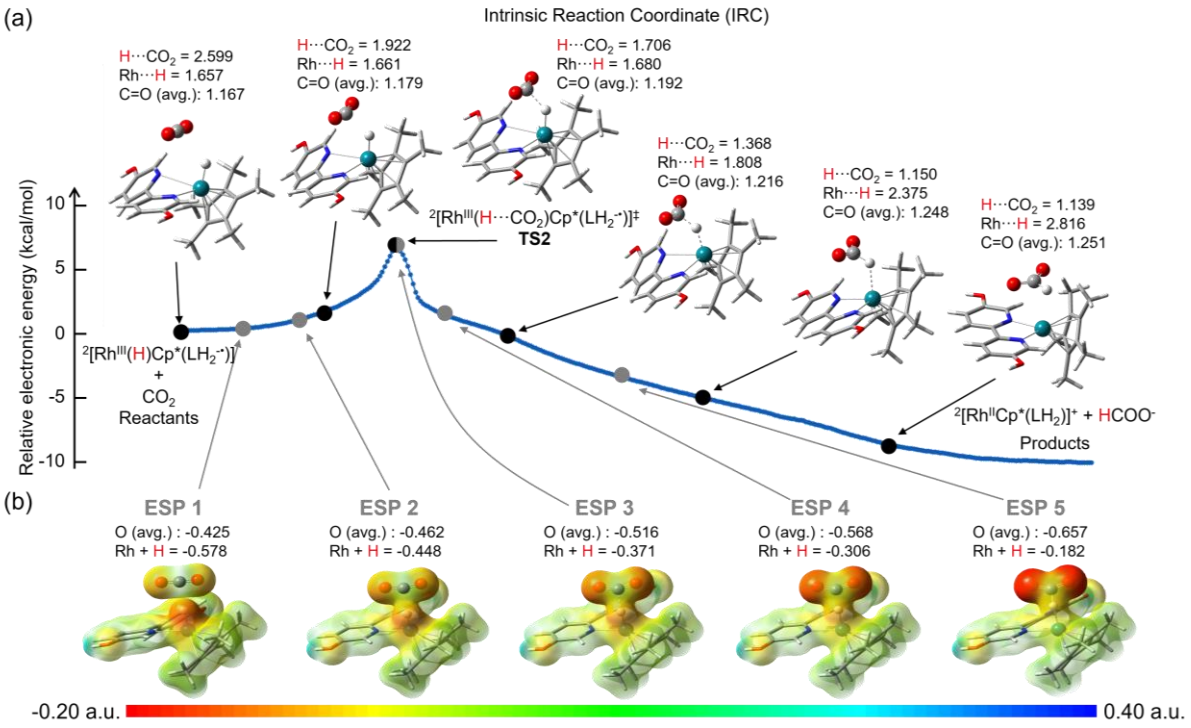

Figure 9. (a) IRC for the transition state of the hydride transfer process with **RhCp*(55dobpyH₂)** at $^{2}[Rh^{III}(H\cdots CO_2)Cp^{*}(LH_{2}^{-\bullet})]^{\ddagger}$. (b) Illustration of electron density from the total SCF density mapped with ESP. Calculation conditions are same to those described in Figure 4. The blue and red surfaces represent the highest (fewer electrons) and lowest (more electrons) ESP, respectively. Isovalue of ESP mapped model is 0.015.

https://doi.org/10.26434/chemrxiv-2024-t3ltd-v3 **ORCID:** https://orcid.org/0000-0003-4976-9796 Content not peer-reviewed by ChemRxiv. **License:** CC BY-NC-ND 4.0

Finally, to clearly understand the hydride transfer step until the $HCOO^-$ is released, the IRC and electrostatic potential (ESP) calculations with regard to the **TS2** of the **RhCp*(55dobpyH$_2$)** derivative were conducted (Figure 9a). As CO_2 approaches to the hydride, the Rh-H bond length slightly increases, with concomitant rise in the average C=O bond length. By viewing the ESP by mapping the electron density, an intriguing shift of electron density from the rhodium-hydride to CO_2 can be recognized (Figure 9b). Particularly noteworthy is the increase in electron density on the oxygen atoms of CO_2 by shifting from **ESP1** to **ESP5**, indicating that the approach results in the transfer of electron density from the hydride to the CO_2 fragment, clearly demonstrating that the $HCOO^-$ formation proceeds simply *via* the transfer of a hydride to CO_2 and ends up by kicking out the $HCOO^-$ without forming a bond to the Rh center. We can thus conclude that the formate formation by the **RhCp*(dobpyH$_2$)** catalysts is not defined as the so-called CO_2 insertion but proceeds *via* the simple addition of hydride to CO_2 according to the Type-D mechanism defined in Scheme 1.

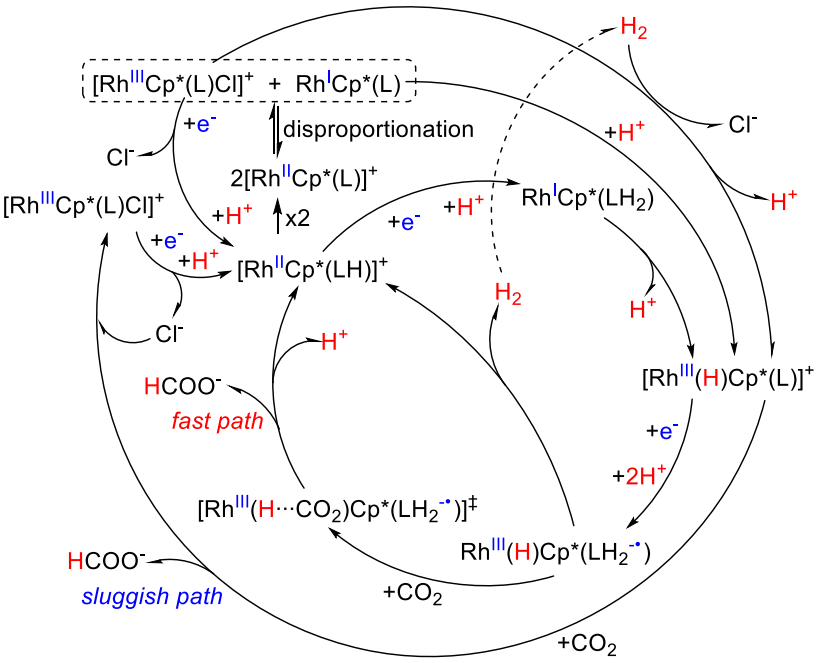

Scheme 5. Schematic representations for the HCOOH production processes catalyzed by the **RhCp*(dobpyH$_2$)** derivatives, clarifying the role of H_2-consumption pathway in competition with the purely photocatalytic pathway.

https://doi.org/10.26434/chemrxiv-2024-t3ltd-v3 **ORCID:** https://orcid.org/0000-0003-4976-9796 Content not peer-reviewed by ChemRxiv. **License:** CC BY-NC-ND 4.0

Based on our DFT and experimental results, the overall mechanism of the highly selective CO_2-to-HCOOH conversion catalyzed by **RhCp*(dobpyH$_2$)** derivatives in the water-added media can be proposed in Scheme 5. The primary catalytic cycle proceeds in a purely photocatalytic fashion *via* the protonated 3-electron-reduced intermediate $Rh^{III}(H)Cp^*(LH_2^{-\bullet})$, which is generated through the additional 1-electron reduction of the non-bpy-reduced $[Rh^{III}(H)Cp^*(L)]^-$. The formate formation *via* the attack on CO_2 by $Rh^{III}(H)Cp^*(LH_2^{-\bullet})$ is regarded as a fast catalytic pathway. On the other hand, the non-bpy-reduced $[Rh^{III}(H)Cp^*(L)]^-$ can also be formed in the dark reaction *via* consumption of the *in-situ* generated H_2 by utilizing the oxo group as a proton relay site in combination with the water-assisted proton transfer processes. The promotion of this H_2-consumption pathway well rationalizes the substantial loss in the yield of H_2 in the water-added systems. Scheme 5 also illustrates that the formate formation *via* the attack on CO_2 by $[Rh^{III}(H)Cp^*(L)]^-$ does not play a significant role under the photocatalytic conditions.

CONCLUSIONS

The present study demonstrates the impact of electronic and steric factors of two hydroxyl functional groups introduced into the bipyridyl ligand of the **RhCp*(bpy)**-type catalysts with regard to the activity and selectivity for CO_2-to-HCOOH conversion. Through a combination of experimental and computational approaches, we have successfully gained profound insights into the effects of water and the hydroxyl functional groups of the catalysts in CO_2 reduction. The most remarkable finding is the dramatic increase in both the yield and selectivity of formate upon switching the solvent from the purely organic to aqueous/organic system. Our study for the first time reveals that the CO_2 reduction to formate proceeds not only *via* the purely photocatalytic route but also *via* the H_2-consumption route bypassing the formation of the non-bpy-reduced hydride intermediate. The unique redox- and ligand-dependent pK_a values of several possible catalyst intermediates together with the dependence of hydricity on the protonation state of dihydroxyl groups have been investigated in detail. Our DFT results

https://doi.org/10.26434/chemrxiv-2024-t3ltd-v3 **ORCID:** https://orcid.org/0000-0003-4976-9796 Content not peer-reviewed by ChemRxiv. **License:** CC BY-NC-ND 4.0

also unveil the exceptionally large canting of the bipyridyl plane due to the steric congestion caused by the 6,6'-dihydroxyl groups, indicative of the destabilized nature of the Rh^{I} and $Rh^{III}(H)$ species of this derivative. This situation not only explains the reason for the cathodically shifted Rh^{III}/Rh^{I} reduction potential but also rationalizes the fast catalytic rate together with the earlier degradation of the 6,6'-substituted derivative. Additionally, it can be correlated to the results of electrochemical study which showed the exceptional reactivity of 6,6'-substituted Rh^{I} species with CO_2. Moreover, the 6,6'-substituted derivative is found to exhibit the highest performance in the heterolytic H_2 cleavage leading to evolve the $Rh^{III}(H)$ species by utilizing the proton-relaying oxo group positioned in close proximity to the H_2-activating Rh^{I} center. We have also elucidated the mechanism of hydride transfer and the intermediates formed during the photocatalysis in detail. All these findings underscore the valuable insights derived from our research and will help further advance the chemistry and technologies in the field of artificial photosynthesis.

EXPERIMENTAL SECTION

Materials and Reagents. Rhodium trichloride ($RhCl_3 \cdot 3H_2O$) was supplied from Tanaka Kikinzoku Kogyo Co., Ltd. 4,4'-Dihydroxy-2,2'-bipyridine (44dobpyH_2), 5,5'-dihydroxy-2,2'-bipyridine (55dobpyH_2), and 6,6'-dihydroxy-2,2'-bipyridine (66dobpyH_2) were purchased from Tokyo Chemical Industry Co., Ltd., and were used as received. BIH was prepared as previously described.[31c] All other reagents were purchased from Kanto Chemicals Co., Inc. and were used without further purification. All solvents were of the highest quality available and were used as received. Purification of water was performed with an Advantec RFD250RB water distillation apparatus.

Measurements. UV-visible absorption spectra were recorded on a Shimadzu UV2450SIM or Shimadzu UV3600 spectrophotometer, where measurement solutions were thermostatted at 20 °C. Electrospray ionization mass spectra (ESI-MS) were recorded on a JEOL JMS-T100LC mass spectrometer in the positive ion mode. In order to confirm the stability of chemical species during the photocatalysis,

https://doi.org/10.26434/chemrxiv-2024-t3ltd-v3 **ORCID:** https://orcid.org/0000-0003-4976-9796 Content not peer-reviewed by ChemRxiv. **License:** CC BY-NC-ND 4.0

cationic species in the reaction mixture were deposited by adding a large excess of an aqueous saturated $NaBPh_4$ (sodium tetraphenylborate) solution to once isolate their solid samples, which were then subjected for the ESI-MS analysis. ^{1}H NMR spectra were acquired on a JEOL JNM-ESA 600 MHz spectrometer. Cyclic voltametric experiments were recorded on a BAS ALS Model 602DKM electrochemical analyzer using a three-electrode system consisting of a glassy carbon working electrode, a platinum wire counter electrode, and an Ag/Ag^+ reference electrode. All the potentials reported are given relative to Fc/Fc^+. The quantification of gaseous products was carried out using a Shimadzu GC-14A gas chromatograph equipped with a molecular sieve 13X-S Å column of 2 m × 3 mm i.d. at 50 °C. The injection of each sample gas (200 μL) was performed manually using a gastight syringe, and the output signal from the thermal conductivity detector (TCD) was analyzed using a Shimadzu C-R8A integrator. The quantification of formate was carried out using a Metrohm 761 Compact IC ion chromatograph. Photoirradiation experiments were carried out using an ILC Technology CERMAX LX-300 Xe lamp equipped with a CM-1 cold mirror that reflects the lights in the range of $\lambda > 400$ nm. The photolysis vial (21 mL) was immersed in a 20 °C water bath to remove IR radiation and to eliminate the temperature effects.

Photocatalytic Experiments. Typically, a 5-mL solution containing **RhCp*(dobpyH$_2$)** (0.1 mM), $[Ru(bpy)_3]Cl_2$•$6H_2O$ (1.0 mM), and BIH (0.1 M) was purged with CO_2 for 30 min prior to irradiation, where two types of solvent conditions were adopted, as noted in the captions in Figure 3. The analysis of the products in the gaseous and liquid phases were carried out by separately preparing the photolysis solutions under the same conditions.

DFT Calculations. DFT calculations were performed using the Gaussian09 software package[43a] to better understand the structural and spin-state candidates and also to computationally determine the redox potentials and the pK_a values of the reaction intermediates supposed to participate in the reactions. The structures of the **RhCp*(dobpyH$_2$)** derivatives were fully optimized using the M06[43b] functional with the effect of solvation in MeCN taken into consideration using the conductor-like polarizable continuum model (C-PCM) method.[44] The use of M06 theory of DFT was reported to show good

https://doi.org/10.26434/chemrxiv-2024-t3ltd-v3 **ORCID:** https://orcid.org/0000-0003-4976-9796 Content not peer-reviewed by ChemRxiv. **License:** CC BY-NC-ND 4.0

consistency with theoretical and experimental results for metal complexes having either redox innocent or non-innocent ligands.[45] Calculations were performed by applying the SDD basis set for the Rh atom with the 6-31G* basis set applied to the rest of atoms (Cl, O, N, C, and H). The pK_a values used to develop the free energy diagrams (Figures 8, S18, and S19) were determined using isodesmic reaction methods[20,46] based on the pK_a value reported for $[TEOA(H)]^+$ (pK_a =15.9 in acetonitrile[32]). The pK_a values of $dobpyH_2$ in different redox intermediates listed in Table 2 were computed using the CAM-B3LYP/SDD(Rh)/6-311+G*(others) level with the solvation model based on density (SMD[47]), as recently indicated to be efficient.[48] For these calculations, the values were benchmarked using the experimentally determined pK_{a1} value of each $[Rh^{III}Cp^*(dobpyH_2)Cl]^+$ catalyst. The redox potentials were also determined using isodesmic reaction methods[20,46] based on the potential value for the process ($[Rh^{III}Cp^*(55dobpyH_2)Cl]^+ + e^- \rightarrow [Rh^{II}Cp^*(55dobpyH_2)]^+ + Cl^-$) supposed to be -0.89 V vs. Fc/Fc^+ in acetonitrile. Structures of transition states were determined using the TS option in Gaussian. The thermodynamic hydricity of $^1[Rh^{III}(H)Cp^*(dobpyH_2)]^+$ and $^2[Rh^{III}(H)Cp^*(dobpyH_2^{-\bullet})]$ was calculated according to the hydride transfer method[34] by employing the hydricity value of formate as 44.2 kcal/mol.[41] ESP-derived charges were computed using the Merz-Kollman-Singh scheme with the MKUFF option in Gaussian, which conducts the MK fitting with UFF radii.[49] Graphical representations were generated using GaussView 6.1.[50]

Synthesis of $[RhCp^*(44dobpyH_2)Cl]Cl\cdot{}^1/_2H_2O$. $[RhCp^*Cl_2]_2$ (0.031 g, 0.05 mmol), prepared by the literature method,[51] and $44dobpyH_2$ (0.021 g, 0.11 mmol) are dissolved in MeOH (2 mL) and refluxed for 2 h, leading to afford an orange solution with no dispersion. The reaction mixture was concentrated by evaporation under reduced pressure followed by addition of an excess of a 8:2 mixture of diethyl ether and ethanol to yield an orange precipitate of the complex, which was collected by filtration and dried under vacuum (yield: 0.039 g, 71%): ^{1}H-NMR (600 MHz, DMSO-d_6) δ 1.62 (s, 15H), 7.25 (d, 2H), 7.85 (d, 2H), 8.58 (d, 2H), 12.24 (bs, 2H) (Figure S2). ESI-MS(+) (MeOH) m/z calcd. for $C_{20}H_{22}N_2O_2Rh$ 425.08; found 425.04 (M^+), 461.05 ($[M]^{2+}+Cl^-$) (Figure S6). Anal. Calcd (%) for $C_{20}H_{23}N_2O_2RhCl_2\cdot{}^1/_2H_2O$ (506.05): C, 47.55; H, 4.59; N, 5.54; found: C, 47.23; H, 4.64; N, 5.06.

https://doi.org/10.26434/chemrxiv-2024-t3ltd-v3 **ORCID:** https://orcid.org/0000-0003-4976-9796 Content not peer-reviewed by ChemRxiv. **License:** CC BY-NC-ND 4.0

Synthesis of [RhCp*(55dobpyH$_2$)Cl]Cl·H$_2$O. This was prepared in the same manner as [RhCp*(44dobpyH$_2$)Cl]Cl using [RhCp*Cl$_2$]$_2$ (0.031 g, 0.05 mmol) and 55dobpyH$_2$ (0.021 g, 0.11 mmol) as starting materials (yield: 0.039 g, 71%): ^{1}H-NMR (600 MHz, DMSO-d_6) δ 1.65 (s, 15H), 7.60 (d, 2H), 8.30 (d, 2H), 8.43 (s, 2H), 11.4 (bs, 2H) (Figure S3). ESI-MS(+) (MeOH) m/z calcd. for $C_{20}H_{22}N_2O_2Rh$ 425.08; found 425.09 (M^+), 461.09 ($[M]^{2+}$+Cl^-) (Figure S7). Anal. Calcd (%) for $C_{20}H_{23}N_2O_2RhCl_2·H_2O$ (515.05): C, 46.62; H, 4.89; N, 5.44; found: C, 46.58; H, 4.91; N, 5.46.

Synthesis of [RhCp*(66dobpyH$_2$)Cl]Cl·$^1/_2$H$_2$O. This was prepared in the same manner as [RhCp*(44dobpyH$_2$)Cl]Cl using [RhCp*Cl$_2$]$_2$ (0.031 g, 0.05 mmol) and 66dobpyH$_2$ (0.021 g, 0.11 mmol) as starting materials (yield: 0.038 g, 70%): ^{1}H-NMR (600 MHz, DMSO-d_6) δ 1.54 (s, 15H), 7.09 (d, 2H), 8.00 (s+t, 2H+2H), 12.9 (bs, 2H) (Figure S4). ESI-MS(+) (MeOH) m/z calcd: 425.08 (M^+); found 425.0 (Figure S8). Anal. Calcd (%) for $C_{20}H_{23}N_2O_2RhCl_2·^1/_2H_2O$ (506.05): C, 47.55; H, 4.59; N, 5.54; found: C, 47.79; H, 4.74; N, 5.54.

Synthesis of [RhCp*(bpy)Cl]Cl. This was prepared in the same manner as [RhCp*(44dobpyH$_2$)Cl]Cl using [RhCp*Cl$_2$]$_2$ (0.031 g, 0.05 mmol) and bpy (0.017 g, 0.11 mmol) as starting materials (yield: 0.047 g, 90%): ^{1}H-NMR (600 MHz, DMSO-d_6) δ 1.67 (s, 15H), 7.88 (t, 2H), 8.35 (t, 2H), 8.71 (2, 2H) (Figure S5). Elemental analysis Calcd: (%) for $C_{20}H_{25}N_2Cl_2Rh·H_2O$ (483.24): C, 49.71; H, 5.21; N, 5.80; found: C, 49.72; H, 5.13; N, 5.79.

https://doi.org/10.26434/chemrxiv-2024-t3ltd-v3 **ORCID:** https://orcid.org/0000-0003-4976-9796 Content not peer-reviewed by ChemRxiv. **License:** CC BY-NC-ND 4.0

ACKNOWLEDGEMENTS

This work was supported by JSPS KAKENHI Grant Numbers JP21H01952, JP21K05100, JP22KK0074, JP23H03831, JP24K01500, and JP24K01611. This work was also supported by JST PRESTO Grant Number JPMJPR22QA.

NOTES

The authors declare no competing interests.

ASSOCIATED CONTENT

Supporting Information

Additional data (characterization, photocatalytic experiments, electrochemistry and spectroscopy data, and DFT results).

REFERENCES

(1) Rogelj, J.; Eelzen, M. D.; Höhne, N.; Fransen, T.; Fekete, H.; Winkler, H.; Schaeffer, R.; Sha, F.; Riahi, K.; Meinshausen, M. Paris Agreement Climate Proposals Need a Boost to Keep Warming Well Below 2 °C. *Nature* **2016**, *534*, 631-639.

(2) (a) Takeda, H.; Cometto, C.; Ishitani, O.; Robert, M. Electrons, Photons, Protons and Earth-Abundant Metal Complexes for Molecular Catalysis of CO_2 Reduction. *ACS Catal.* **2017**, *7,* 70-88. (b) Wu, H.-L.; Li, X.-B.; Tung, C.-H.; Wu, L.-Z. Semiconductor Quantum Dots: An Emerging Candidate for CO_2 Photoreduction. *Adv. Mater.* **2019**, *31,* 1900709. (c) Zhang, B.; Sun, L. Artificial Photosynthesis: Opportunities and Challenges of Molecular Catalysts. *Chem. Soc. Rev.* **2019**, *48,* 2216-2264.

(3) (a) Albero, J.; Peng, Y.; García, H. Photocatalytic CO_2 Reduction to C2+ Products. *ACS Catal.* **2020**, *10,* 5734-5749. (b) Song, Y.; Chen, W.; Wei, W.; Sun, Y. Advances in Clean Fuel Ethanol Production from Electro-, Photo- and Photoelectro-Catalytic CO_2 Reduction. *Catalysts* **2020***, 10,* 1287-1312.

(4) (a) Morris, A. J.; Meyer, G. J.; Fujita, E. Molecular Approaches to the Photocatalytic Reduction of Carbon Dioxide for Solar Fuels. *Acc. Chem. Res.* **2009***, 42,* 1983-1994. (b) Barber, J. Photosynthetic

https://doi.org/10.26434/chemrxiv-2024-t3ltd-v3 **ORCID:** https://orcid.org/0000-0003-4976-9796 Content not peer-reviewed by ChemRxiv. **License:** CC BY-NC-ND 4.0

Energy Conversion: Natural and Artificial. *Chem. Soc. Rev.* **2009**, *38*, 185-196. (c) Dalle, K. E.; Warnan, J.; Leung, J. J.; Reuillard, B.; Karmel, I. S.; Reisner, E. Electro- and Solar-Driven Fuel Synthesis with First Row Transition Metal Complexes. *Chem. Rev.* **2019**, *119*, 2752-2875. (d) Xu, S.; Carter, E. A. Theoretical Insights into Heterogeneous (Photo)Electrochemical CO_2 Reduction. *Chem. Rev.* **2019**, *119*, 6631-6669.

(5) (a) Costentin, C.; Drouet, S.; Robert, M.; Saveant, J.-M. A Local Proton Source Enhances CO_2 Electroreduction to CO by a Molecular Fe catalyst. *Science* **2012**, *338*, 90-94. (b) Costentin, C.; Robert, M.; Saveant, J.-M. Current Issues in Molecular Catalysis Illustrated by Iron Porphyrins as Catalysts of the CO_2-to-CO Electrochemical Conversion. *Acc. Chem. Res.* **2015**, *48*, 2996-3006.

(6) (a) Smieja, J. M.; Sampson, M. D.; Grice, K. A.; Benson, E. E.; Froehlich, J. D.; Kubiak, C. P. Manganese as a Substitute for Rhenium in CO_2 Reduction Catalysts: The Importance of Acids. *Inorg. Chem.* **2013**, *52*, 2484-2491. (b) Machan, C. W.; Stanton, C. J.; Vandezande, J. E.; Majetich, G. F.; Schaefer, H. F.; Kubiak, C. P.; Agarwal, J. Electrocatalytic Reduction of Carbon Dioxide by Mn(CN)(2,2′-bipyridine)$(CO)_3$: CN Coordination Alters Mechanism. *Inorg. Chem.* **2015**, *54*, 8849-8856.

(7) (a) Beley, M.; Collin, J.-P.; Ruppert, R.; Sauvage, J.-P. Nickel(II)-cyclam: an Extremely Selective Electrocatalyst for Reduction of CO_2 in Water. *J. Chem. Soc., Chem. Commun.* **1984**, *19*, 1315-1316. (b) Froehlich, J. D.; Kubiak, C. P. Homogeneous CO_2 Reduction by Ni(cyclam) at a Glassy Carbon Electrode. *Inorg. Chem.* **2012**, *51*, 3932-3934. (c) Schneider, J.; Jia, H.; Kobiro, K.; Cabelli, D. E.; Muckerman, J. T.; Fujita, E. Nickel(II) Macrocycles: Highly Efficient Electrocatalysts for the Selective Reduction of CO_2 to CO. *Energy Environ. Sci.* **2012**, *5*, 9502-9510. (d) Song, J.; Klein, E. L.; Neese, F.; Ye, S. The Mechanism of Homogeneous CO_2 Reduction by Ni(cyclam): Product Selectivity, Concerted Proton-Electron Transfer and C-O Bond Cleavage. *Inorg. Chem.* **2014**, *53*, 7500-7507. (e) Froehlich, J. D.; Kubiak, C. P. The Homogeneous Reduction of CO_2 by $[Ni(cyclam)]^+$: Increased Catalytic Rates with the Addition of a CO Scavenger. *J. Am. Chem. Soc.* **2015**, *137*, 3565-3573. (f)

https://doi.org/10.26434/chemrxiv-2024-t3ltd-v3 **ORCID:** https://orcid.org/0000-0003-4976-9796 Content not peer-reviewed by ChemRxiv. **License:** CC BY-NC-ND 4.0

Schneider, C. R.; Lewis, L. C.; Shafaat, H. S. The good, the Neutral, and the Positive: Buffer Identity Impacts CO_2 Reduction Activity by Nickel(II) Cyclam. *Dalton Trans.* **2019**, *48*, 15810-15821.

(8) Call, A.; Cibian, M.; Yamamoto, K.; Nakazono, T.; Yamauchi, K.; Sakai, K. Highly Efficient and Selective Photocatalytic CO_2 Reduction to CO in Water by a Cobalt Porphyrin Molecular Catalyst. *ACS Catal.* **2019**, *9*, 4867-4874.

(9) Yue, M.; Lambert, H.; Pahon, E.; Roche, R.; Jemei, S.; Hissel, D. Hydrogen Energy Systems: A Critical Review of Technologies, Applications, Trends and Challenges. *Renewable Sustainable Energy Rev.* **2021**, *146*, 111180.

(10) Mellmann, D.; Sponholz, P.; Junge, H.; Beller, M. Formic Acid as a Hydrogen Storage Material-Development of Homogeneous Catalysts for Selective Hydrogen Release. *Chem. Soc. Rev.* **2016**, *45*, 3954-3988.

(11) Elgrishi, N.; Chambers, M. B.; Wang, X.; Fontecave, M. Molecular Polypyridine-based Metal Complexes as Catalysts for the Reduction of CO_2. *Chem. Soc. Rev.* **2017**, *46*, 761-796.

(12) (a) Nakada, A.; Koike, K.; Nakashima, T.; Morimoto, T.; Ishitani, O. Photocatalytic CO_2 Reduction to Formic Acid Using a Ru(II)-Re(I) Supramolecular Complex in an Aqueous Solution. *Inorg. Chem.* **2015**, *54*, 1800-1807. (b) Clark, M. L.; Cheung, P. L.; Lessio, M.; Carter, E. A.; Kubiak, C. P. Kinetic and Mechanistic Effects of Bipyridine (bpy) Substituent, Labile Ligand, and Brønsted Acid on Electrocatalytic CO_2 Reduction by Re(bpy) Complexes. *ACS Catal.* **2018**, *8*, 2021-2029.

(13) (a) Rodrigues, R. R.; Boudreaux, C. M.; Papish, E. T.; Delcamp, J. H. Photocatalytic Reduction of CO_2 to CO and Formate: Do Reaction Conditions or Ruthenium Catalysts Control Product Selectivity?. *ACS Appl. Energy Mater.* **2019**, *2*, 37-46. (b) Ho, P.-Y.; Cheng, S.-C.; Yu, F.; Yeung, Y.-Y.; Ni, W.-X.; Ko, C.-C.; Leung, C.-F.; Lau, T.-C.; Robert, M. Light-Driven Reduction of CO_2 to CO in Water with a Cobalt Molecular Catalyst and an Organic Sensitizer. *ACS Catal.* **2023**, *13*, 5979-5985.

(14) (a) Kaufhold, S.; Petermann, L.; Staehle, R.; Rau, S. Transition Metal Complexes with N-heterocyclic Carbene Ligands: From Organometallic Hydrogenation Reactions toward Water Splitting. *Coord. Chem. Rev.* **2015**, *304-305*, 73-87. (b) Mengele, A. K.; Rau, S. Product Selectivity in

https://doi.org/10.26434/chemrxiv-2024-t3ltd-v3 **ORCID:** https://orcid.org/0000-0003-4976-9796 Content not peer-reviewed by ChemRxiv. **License:** CC BY-NC-ND 4.0

Homogeneous Artificial Photosynthesis Using [(bpy)Rh(Cp*)X]$^{n+}$-Based Catalysts. *Inorganics* **2017**, *5*, 35.

(15) (a) Zhang, X.; Cibian, M.; Call, A.; Yamauchi, K.; Sakai, K. Photochemical CO_2 Reduction Driven by Water-Soluble Copper(I) Photosensitizer with the Catalysis Accelerated by Multi-Electron Chargeable Cobalt Porphyrin. *ACS Catal.* **2019**, 9, 11263-11273. (b) Zhang, X.; Yamauchi, K.; Sakai, K. Earth-Abundant Photocatalytic CO_2 Reduction by Multielectron Chargeable Cobalt Porphyrin Catalysts: High CO/H_2 Selectivity in Water Based on Phase Mismatch in Frontier MO Association. *ACS Catal*. **2021**, *11*, 10436-10449.

(16) (a) Pugliese, E.; Gotico, P.; Wehrung, I.; Boitrel, B.; Quaranta, A.; Ha-Thi, M.-H.; Pino, T.; Sircoglou, M.; Leibl, W.; Halime, Z.; Aukauloo, A. Dissection of Light-Induced Charge Accumulation at a Highly Active Iron Porphyrin: Insights in the Photocatalytic CO_2 Reduction. *Angew. Chem. Int. Ed.* **2022**, *61*, e202117530. (b) Zhang, C.; Gotico, P.; Guillot, R.; Dragoe, D.; Leibl, W.; Halime, Z.; Aukauloo, A. Bio-Inspired Bimetallic Cooperativity Through a Hydrogen Bonding Spacer in CO_2 Reduction. *Angew. Chem. Int. Ed.* **2023**, *62*, e202214665. (c) Amanullah, S.; Gotico, P.; Sircoglou, M.; Leibl, W.; Llansola-Portoles, M. J.; Tibiletti, T.; Quaranta, A.; Halime, Z.; Aukauloo, A. Second Coordination Sphere Effect Shifts CO_2 to CO Reduction by Iron Porphyrin from Fe^0 to Fe^I. *Angew. Chem. Int. Ed.* **2024**, *63*, e202314439.

(17) (a) Sullivan, B. P.; Meyer, T. J. Kinetics and Mechanism of Carbon Dioxide Insertion into a Metal-Hydride Bond. A Large Solvent Effect and an Inverse Kinetic Isotope Effect. *Organometallics* **1986**, *5*, 1500-1502. (b) Pugh, J. R.; Bruce, M. R. M.; Sullivan, B. P.; Meyer, T. J. Formation of a Metal-Hydride Bond and the Insertion of CO_2. Key Steps in the Electrocatalytic Reduction of Carbon Dioxide to Formate Anion. *Inorg. Chem.* **1991**, *30*, 86-91. (c) Tanaka, R.; Yamashita, M.; Nozaki, K. Catalytic Hydrogenation of Carbon Dioxide Using Ir(III)-Pincer Complexes. *J. Am. Chem. Soc.* **2009**, *131*, 14168-14169. (d) Ziebart, C.; Federsel, C.; Anbarasan, P.; Jackstell, R.; Baumann, W.; Spannenberg, A.; Beller, M. Well-Defined Iron Catalyst for Improved Hydrogenation of Carbon Dioxide and Bicarbonate. *J. Am. Chem. Soc.* **2012**, *134*, 20701-20704. (e) Hull, J. F.; Himeda, Y.; Wang, W. H.;

https://doi.org/10.26434/chemrxiv-2024-t3ltd-v3 **ORCID:** https://orcid.org/0000-0003-4976-9796 Content not peer-reviewed by ChemRxiv. **License:** CC BY-NC-ND 4.0

Hashiguchi, B.; Periana, R.; Szalda, D. J.; Muckerman, J. T.; Fujita, E. Reversible Hydrogen Storage Using CO_2 and a Proton-Switchable Iridium Catalyst in Aqueous Media under Mild Temperatures and Pressures. *Nat. Chem.* **2012**, *4*, 383-388. (f) Lilio, A. M.; Reineke, M. H.; Moore, C. E.; Rheingold, A. L.; Takase, M. K.; Kubiak, C. P. Incorporation of Pendant Bases into Rh(diphosphine)$_2$ Complexes: Synthesis, Thermodynamic Studies, and Catalytic CO_2 Hydrogenation Activity of $[Rh(P_2N_2)_2]^+$ Complexes. *J. Am. Chem. Soc.* **2015**, *137*, 8251-8260. (g) Waldie, K. M.; Brunner, F. M.; Kubiak, C. P. Transition Metal Hydride Catalysts for Sustainable Interconversion of CO_2 and Formate: Thermodynamic and Mechanistic Considerations. *ACS Sustainable Chem. Eng.* **2018**, *6*, 6841-6848.

(18) (a) Ahlquist, M. S. Iridium Catalyzed Hydrogenation of CO_2 Under Basic Conditions–Mechanistic Insight from Theory. *J. Mol. Catal. A: Chem.* **2010**, *324*, 3-8. (b) Madsen, M. R.; Rønne, M. H.; Heuschen, M.; Golo, D.; Ahlquist, M. S. G.; Skrydstrup, T.; Pedersen, S. U.; Daasbjerg, K. Promoting Selective Generation of Formic Acid from CO_2 Using Mn(bpy)$(CO)_3$Br as Electrocatalyst and Triethylamine/Isopropanol as Additives. *J. Am. Chem. Soc.* **2021**, *143*, 20491-20500.

(19) (a) Schmeier, T. J.; Dobereiner, G. E.; Crabtree, R. H.; Hazari, N. Secondary Coordination Sphere Interactions Facilitate the Insertion Step in an Iridium(III) CO_2 Reduction Catalyst. *J. Am. Chem. Soc.* **2011**, *133*, 9274-9277. (b) Hazari, N.; Heimann, J. E. Carbon Dioxide Insertion into Group 9 and 10 Metal-Element σ Bonds. *Inorg. Chem.* **2017**, *56*, 13655-13678. (c) Heimann, J. E.; Bernskoetter, W. H.; Hazari, N.; Mayer, J. M. Acceleration of CO_2 Insertion into Metal Hydrides: Ligand, Lewis Acid, and Solvent Effects on Reaction Kinetics. *Chem. Sci.* **2018**, *9*, 6629-6638.

(20) Liao, C.; Yamauchi, K.; Sakai, K. Mechanism of Ni-NHC CO_2 Reduction Catalysis Predominantly Affording Formate via Attack of Metal Hydride to CO_2. *ACS Catal.* **2024**, *14*, 11131-11137.

(21) (a) Ishida, H.; Tanaka, K.; Tanaka, T., Electrochemical CO_2 Reduction Catalyzed by Ruthenium Complexes $[Ru(bpy)_2(CO)_2]^{2+}$ and $[Ru(bpy)_2(CO)Cl]^+$. Effect of pH on the Formation of CO and $HCOO^-$. *Organometallics* **1987,** *6*, 181-186. (b) Guo, Z.; Chen, G.; Cometto, C.; Ma, B.; Zhao, H.; Groizard, T.; Chen, L.; Fan, H.; Man, W.-L.; Yiu, S.-M.; Lau, K.-C.; Lau, T.-C.; Robert, M. Selectivity Control of CO versus $HCOO^-$ Production in the Visible-Light-Driven Catalytic Reduction of CO_2 with

https://doi.org/10.26434/chemrxiv-2024-t3ltd-v3 **ORCID:** https://orcid.org/0000-0003-4976-9796 Content not peer-reviewed by ChemRxiv. **License:** CC BY-NC-ND 4.0

Two Cooperative Metal Sites. *Nat. Catal.* **2019**, *2*, 801-808. (c) Amanullah, S.; Saha, P.; Dey, A. Activating the Fe(I) State of Iron Porphyrinoid with Second-Sphere Proton Transfer Residues for Selective Reduction of CO_2 to HCOOH via Fe(III/II)-COOH Intermediate(s). *J. Am. Chem. Soc.* **2021**, *143*, 13579-13592. (d) Bharti, J.; Chen, L.; Guo, Z.; Cheng, L.; Wellauer, J.; Wenger, O. S.; von Wolff, N.; Lau, K. C.; Lau, T. C.; Chen, G.; Robert, M. Visible-Light-Driven CO_2 Reduction with Homobimetallic Complexes. Cooperativity between Metals and Activation of Different Pathways. *J. Am. Chem. Soc.* **2023**, *145*, 25195-25202.

(22) (a) Immirzi, A.; Musco, A. Reactions of *trans*-{$PtH_2[PtH_2[P(C_6H_{11})_3]_2$} with Carbon Dioxide. X-Ray Structures of trans-{$PtH(O_2CH)[P(C_6H_{11})_3]_2$} and *trans*-{$PtH(O_2COCH_3)[P(C_6H_{11})_3]_2$}. *Inorg. Chim. Acta.* **1977,** *22*, L35-L36. (b) Whittlesey, M. K.; Perutz, R. N.; Moore, M. H. Facile Insertion of CO_2 into the Ru−H Bonds of $Ru(dmpe)_2H_2$ (dmpe = $Me_2PCH_2CH_2PMe_2$): Identification of Three Ruthenium Formate Complexes. *Organometallics* **1996,** *15*, 5166-5169. (c) Williams, M. T.; McEachin, C.; Becker, T. M.; Ho, D. M.; Mandal, S. K. Synthesis and X-ray Structures of Manganese(I) and Rhenium(I) Formato Complexes, *fac*-$(CO)_3$(dppp)M-OC(H)O. *J. Organomet. Chem.* **2000,** *599*, 308-312. (d) Langer, R.; Diskin-Posner, Y.; Leitus, G.; Shimon, L. J.; Ben-David, Y.; Milstein, D. Low-Pressure Hydrogenation of Carbon Dioxide Catalyzed by an Iron Pincer Complex Exhibiting Noble Metal Activity. *Angew. Chem. Int. Ed.* **2011**, *50*, 9948-9952. (e) Bertini, F.; Gorgas, N.; Stöger, B.; Peruzzini, M.; Veiros, L. F.; Kirchner, K.; Gonsalvi, L. Efficient and Mild Carbon Dioxide Hydrogenation to Formate Catalyzed by Fe(II) Hydrido Carbonyl Complexes Bearing 2,6-(Diaminopyridyl)diphosphine Pincer Ligands. *ACS Catal.* **2016**, *6*, 2889-2893. (f) Anaby, A.; Feller, M.; Ben-David, Y.; Leitus, G.; Diskin-Posner, Y.; Shimon, L. J. W.; Milstein, D. Bottom-Up Construction of a CO_2-Based Cycle for the Photocarbonylation of Benzene, Promoted by a Rhodium(I) Pincer Complex. *J. Am. Chem. Soc.* **2016**, *138*, 9941-9950.

(23) (a) Jeletic, M. S.; Mock, M. T.; Appel, A. M.; Linehan, J. C. A Cobalt-Based Catalyst for the Hydrogenation of CO_2 under Ambient Conditions. *J. Am. Chem. Soc.* **2013**, *135*, 11533-11536. (b) Roy, S.; Sharma, B.; Pécaut, J.; Simon, P.; Fontecave, M.; Tran, P. D.; Derat, E.; Artero, V. Molecular Cobalt

https://doi.org/10.26434/chemrxiv-2024-t3ltd-v3 **ORCID:** https://orcid.org/0000-0003-4976-9796 Content not peer-reviewed by ChemRxiv. **License:** CC BY-NC-ND 4.0

Complexes with Pendant Amines for Selective Electrocatalytic Reduction of Carbon Dioxide to Formic Acid. *J. Am. Chem. Soc.* **2017**, *139*, 3685-3696. (c) Zhu, C.-Y.; Zhang, Y.-Q.; Liao, R.-Z.; Xia, W.; Hu, J.-C.; Wu, J.; Liu, H.; Wang, F. Photocatalytic Reduction of CO_2 to CO and Formate by a Novel Co(II) Catalyst Containing a *cis*-Oxygen Atom: Photocatalysis and DFT Calculations. *Dalton Trans.* **2018**, *47*, 13142-13150. (d) Todorova, T. K.; Huan, T. N.; Wang, X.; Agarwala, H.; Fontecave, M. Controlling Hydrogen Evolution during Photoreduction of CO_2 to Formic Acid Using $[Rh(R\text{-}Bpy)(Cp^*)Cl]^+$ Catalysts: A Structure-Activity Study. *Inorg. Chem.* **2019**, *58*, 6893-6903. (e) Vichou, E.; Solé-Daura, A.; Mellot-Draznieks, C.; Li, Y.; Gomez-Mingot, M.; Fontecave, M.; Sánchez-Sánchez, C. M. Electrocatalytic Conversion of CO_2 to Formate at Low Overpotential by Electrolyte Engineering in Model Molecular Catalysis. *ChemSusChem* **2022**, *15*, e202201566.

(24) Call, A.; Cibian, M.; Yamauchi, K.; Sakai, K. Visible-light-driven Reduction of CO_2 to CO in Fully Aqueous Media Using a Water-soluble Cobalt Porphyrin. *Sustainable Energy Fuels* **2022**, *6*, 2160-2164.

(25) Wang, J. W.; Yamauchi, K.; Huang, H. H.; Sun, J. K.; Luo, Z. M.; Zhong, D. C.; Lu, T. B.; Sakai, K. Molecular Cobalt Hydrogen Evolution Catalyst Showing High Activity and Outstanding Tolerance to CO and O_2. *Angew. Chem. Int. Ed.* **2019**, *58*, 10923-10927.

(26) Himeda, Y.; Onozawa-Komatsuzaki, N.; Sugihara, H.; Kasuga, K. Simultaneous Tuning of Activity and Water Solubility of Complex Catalysts by Acid-Base Equilibrium of Ligands for Conversion of Carbon Dioxide. *Organometallics* **2007**, *26*, 702-712.

(27) (a) Ogo, S.; Kabe, R.; Hayashi, H.; Harada, R.; Fukuzumi, S. Mechanistic Investigation of CO_2 Hydrogenation by Ru(II) and Ir(III) Aqua Complexes Under Acidic Conditions: Two Catalytic Systems Differing in the Nature of the Rate Determining Step. *Dalton Trans.* **2006**, 4657-4663. (b) Wang, W.-H.; Muckerman, J. T.; Fujita, E.; Himeda, Y. Mechanistic Insight through Factors Controlling Effective Hydrogenation of CO_2 Catalyzed by Bioinspired Proton-Responsive Iridium(III) Complexes. *ACS Catal.* **2013**, *3,* 856-860.

https://doi.org/10.26434/chemrxiv-2024-t3ltd-v3 **ORCID:** https://orcid.org/0000-0003-4976-9796 Content not peer-reviewed by ChemRxiv. **License:** CC BY-NC-ND 4.0

(28) Caix, C.; Chardon-Noblat, S.; Deronzier, A. Electrocatalytic Reduction of CO_2 into Formate with $[(\eta^5\text{-}Me_5C_5)M(L)Cl]^+$ Complexes (L=2,2′-bipyridine ligands; M=Rh(III) and Ir(III)). *J. Electroanal. Chem.* **1997**, *434*, 163-170.

(29) Troian-Gautier, L.; Moucheron, C. Ruthenium^{II} Complexes Bearing Fused Polycyclic Ligands: From Fundamental Aspects to Potential Applications. *Molecules* **2014**, *19*, 5028-5087.

(30) Connelly, N. G.; Geiger, W. E. Chemical Redox Agents for Organometallic Chemistry. *Chem. Rev.* **1996**, *96,* 877-910.

(31) (a) Tamaki, Y.; Koike, K.; Morimoto, T.; Ishitani, O. Substantial Improvement in the Efficiency and Durability of a Photocatalyst for Carbon Dioxide Reduction Using a Benzoimidazole Derivative as an Electron Donor. *J. Catal.* **2013**, *304*, 22-28. (b) Morimoto, T.; Nakajima, T.; Sawa, S.; Nakanishi, R.; Imori, D.; Ishitani, O. CO_2 Capture by a Rhenium(I) Complex with the Aid of Triethanolamine. *J. Am. Chem. Soc.* **2013**, *135*, 16825-16828. (c) Tamaki, Y.; Koike, K.; Ishitani, O. Highly Efficient, Selective, and Durable Photocatalytic System for CO_2 Reduction to Formic Acid. *Chem. Sci*. **2015**, *6*, 7213-7221. (d) Sampaio, R. N.; Grills, D. C.; Polyansky, D. E.; Szalda, D. J.; Fujita, E. Unexpected Roles of Triethanolamine in the Photochemical Reduction of CO_2 to Formate by Ruthenium Complexes. *J. Am. Chem. Soc.* **2020**, *142*, 2413-2428.

(32) Izutsu, K.; Nakamura, T.; Takizawa, K.; Takeda, A. Calorimetric Determination of Thermodynamic Parameters for the Dissociations of Acids in Dipolar Aprotic Solvents. *Bull. Chem. Soc. Jpn.* **1985**, *58*, 455-458.

(33) (a) Himeda, Y. Conversion of CO_2 into Formate by Homogeneously Catalyzed Hydrogenation in Water: Tuning Catalytic Activity and Water Solubility through the Acid-Base Equilibrium of the Ligand. *Eur. J. Inorg. Chem.* **2007**, 3927-3941. (b) Himeda, Y.; Onozawa-Komatsuzaki, N.; Miyazawa, S.; Sugihara, H.; Hirose, T.; Kasuga, K. pH-Dependent Catalytic Activity and Chemoselectivity in Transfer Hydrogenation Catalyzed by Iridium Complex with 4,4′-Dihydroxy-2,2′-bipyridine. *Chem. Eur. J.* **2008**, *14*, 11076-11081. (c) Himeda, Y.; Miyazawa, S.; Hirose, T. Interconversion Between Formic Acid and H_2/CO_2 Using Rhodium and Ruthenium Catalysts for CO_2 Fixation and H_2 Storage.

https://doi.org/10.26434/chemrxiv-2024-t3ltd-v3 **ORCID:** https://orcid.org/0000-0003-4976-9796 Content not peer-reviewed by ChemRxiv. **License:** CC BY-NC-ND 4.0

ChemSusChem **2011**, *4*, 487-493. (d) Ertem, M. Z.; Himeda, Y.; Fujita, E.; Muckerman, J. T. Interconversion of Formic Acid and Carbon Dioxide by Proton-Responsive, Half-Sandwich Cp*Ir^{III} Complexes: A Computational Mechanistic Investigation. *ACS Catal.* **2016**, *6*, 600-609. (e) Siek, S.; Burks, D. B.; Gerlach, D. L.; Liang, G.; Tesh, J. M.; Thompson, C. R.; Qu, F.; Shankwitz, J. E.; Vasquez, R. M.; Chambers, N.; Szulczewski, G. J.; Grotjahn, D. B.; Webster, C. E.; Papish, E. T. Iridium and Ruthenium Complexes of N-Heterocyclic Carbene- and Pyridinol-Derived Chelates as Catalysts for Aqueous Carbon Dioxide Hydrogenation and Formic Acid Dehydrogenation: The Role of the Alkali Metal. *Organometallics* **2017**, *36*, 1091-1106. (f) Nijamudheen, A.; Kanega, R.; Onishi, N.; Himeda, Y.; Fujita, E.; Ertem, M. Z. Distinct Mechanisms and Hydricities of Cp*Ir-Based CO_2 Hydrogenation Catalysts in Basic Water. *ACS Catal.* **2021**, *11*, 5776-5788.

(34) Wiedner, E. S.; Chambers, M. B.; Pitman, C. L.; Bullock, R. M.; Miller, A. J. M.; Appel, A. M. Thermodynamic Hydricity of Transition Metal Hydrides. *Chem. Rev.* **2016**, *116*, 8655-8692.

(35) Kubas, G. J. Dihydrogen Complexes as Prototypes for the Coordination Chemistry of Saturated Molecules. *Proc. Natl. Acad. Sci. USA* **2007**, *104*, 6901-6907.

(36) Moore, C. M.; Dahl, E. W.; Szymczak, N. K. Beyond H_2: Exploiting 2-Hydroxypyridine as a Design Element from [Fe]-Hydrogenase for Energy-Relevant Catalysis. *Curr. Opin. Chem. Biol.* **2015**, *25*, 9-17.

(37) DuBois, D. L.; Bullock, R. M. Molecular Electrocatalysts for the Oxidation of Hydrogen and the Production of Hydrogen-The Role of Pendant Amines as Proton Relays. *Eur. J. Inorg. Chem.* **2011**, 1017-1027.

(38) Johnson, S. I.; Gray, H. B.; Blakemore, J. D.; Goddard, W. A. Role of Ligand Protonation in Dihydrogen Evolution from a Pentamethylcyclopentadienyl Rhodium Catalyst. *Inorg. Chem.* **2017**, *56*, 11375-11386.

(39) Quintana, L. M. A.; Johnson, S. I.; Corona, S. L.; Villatoro, W.; Goddard, W. A.; Takase, M. K.; VanderVelde, D. G.; Winkler, J. R.; Gray, H. B.; Blakemore, J. D. Proton-Hydride Tautomerism in Hydrogen Evolution Catalysis. *Proc. Natl. Acad. Sci. USA* **2016**, *113*, 6409-6414.

https://doi.org/10.26434/chemrxiv-2024-t3ltd-v3 **ORCID:** https://orcid.org/0000-0003-4976-9796 Content not peer-reviewed by ChemRxiv. **License:** CC BY-NC-ND 4.0

(40) Pitman, C. L.; Finster, O. N. L.; Miller, A. J. M. Cyclopentadiene-Mediated Hydride Transfer from Rhodium Complexes. *Chem. Commun.* **2016**, *52,* 9105-9108.

(41) Miller, A. J. M.; Labinger, J. A.; Bercaw, J. E. Trialkylborane-Assisted CO_2 Reduction by Late Transition Metal Hydrides. *Organometallics*. **2011**, *30*, 4308-4314.

(42) Ceballos, B. M.; Yang, J. Y. Directing the Reactivity of Metal Hydrides for Selective CO_2 Reduction. *Proc. Natl. Acad. Sci. U. S. A.* **2018**, *115*, 12686-12691.

(43) (a) Frisch, M. J.; et al. Gaussian09, Revision D.01; Gaussian, Inc.: Wallingford, CT, 2009. (b) Zhao, Y.; Truhlar, D. G. The M06 Suite of Density Functionals for Main Group Thermochemistry, Thermochemical Kinetics, Noncovalent Interactions, Excited States, and Transition Elements: Two New Functionals and Systematic Testing of Four M06-class Functionals and 12 Other Functionals. *Theor. Chem. Acc.* **2008**, *120*, 215-241.

(44) Cossi, M.; Rega, N.; Scalmani, G.; Barone, V. Energies, Structures, and Electronic Properties of Molecules in Solution with the C-PCM Solvation Model. *J. Comput. Chem.* **2003**, *24*, 669-681.

(45) (a) Bushnell, E. A. C.; Boyd, R. J. Assessment of Several DFT Functionals in Calculation of the Reduction Potentials for Ni-, Pd-, and Pt-Bis-ethylene-1,2-dithiolene and -Diselenolene Complexes. *J. Phys. Chem. A* **2015**, *119*, 911-918. (b) Coskun, D.; Jerome, S. V.; Friesner, R. A. Evaluation of the Performance of the B3LYP, PBE0, and M06 DFT Functionals, and DBLOC-Corrected Versions, in the Calculation of Redox Potentials and Spin Splittings for Transition Metal Containing Systems. *J. Chem. Theory Comput.* **2016**, *12*, 1121-1128. (c) Johnson, S. I.; Nielsen, R. J.; Goddard, W. A. Selectivity for HCO_2^- over H_2 in the Electrochemical Catalytic Reduction of CO_2 by (POCOP)IrH_2. *ACS Catal.* **2016**, *6*, 6362-6371. (d) Ngo, K. T.; McKinnon, M.; Mahanti, B.; Narayanan, R.; Grills, D. C.; Ertem, M. Z.; Rochford, J. Turning on the Protonation-First Pathway for Electrocatalytic CO_2 Reduction by Manganese Bipyridyl Tricarbonyl Complexes. *J. Am. Chem. Soc.* **2017**, *139*, 2604-2618.

(46) Sakaguchi, Y.; Call, A.; Yamauchi, K.; Sakai, K., Catalysis of CO_2 Reduction by Diazapyridinophane Complexes of Fe, Co, and Ni: CO_2 Binding Triggered by Combined Frontier MO Associations Involving a SOMO. *Dalton Trans.* **2021,** *50*, 15983-15995.

https://doi.org/10.26434/chemrxiv-2024-t3ltd-v3 **ORCID:** https://orcid.org/0000-0003-4976-9796 Content not peer-reviewed by ChemRxiv. **License:** CC BY-NC-ND 4.0

(47) Marenich, A. V.; Cramer, C. J.; Truhlar, D. G., Universal Solvation Model Based on Solute Electron Density and a Continuum Model of the Solvent Defined by the Bulk Dielectric Constant and Atomic Surface Tensions. *J. Phys. Chem. B,* **2009**, *113*, 6378-6396.

(48) Pezzola, S.; Venanzi, M.; Galloni, P.; Conte, V.; Sabuzi, F., Towards the "Eldorado" of pKa Determination: A Reliable and Rapid DFT Model. *Molecules* **2024**, *29*, 1255.

(49) (a) Singh, U. C.; Kollman, P. A. An Approach to Computing Electrostatic Charges for Molecules. *J. Comput. Chem.* **1984,** *5*, 129-145. (b) Besler, B. H.; Merz Jr., K. M.; Kollman, P. A. Atomic Charges Derived from Semiempirical Methods. *J. Comput. Chem.* **1990,** *11*, 431-439.

(50) Dennington, R.; Keith, T. A.; Millam, J. M. *GaussView*, version 6.1; Gaussian Inc., **2019**.

(51) White, C.; Yates, A.; Maitlis, P. M. (η^5-Pentamethylcyclopentadienyl)Rhodium and -Iridium Compounds. *Inorg. Synth.* **1992**, *29*, 228-234.

https://doi.org/10.26434/chemrxiv-2024-t3ltd-v3 **ORCID:** https://orcid.org/0000-0003-4976-9796 Content not peer-reviewed by ChemRxiv. **License:** CC BY-NC-ND 4.0